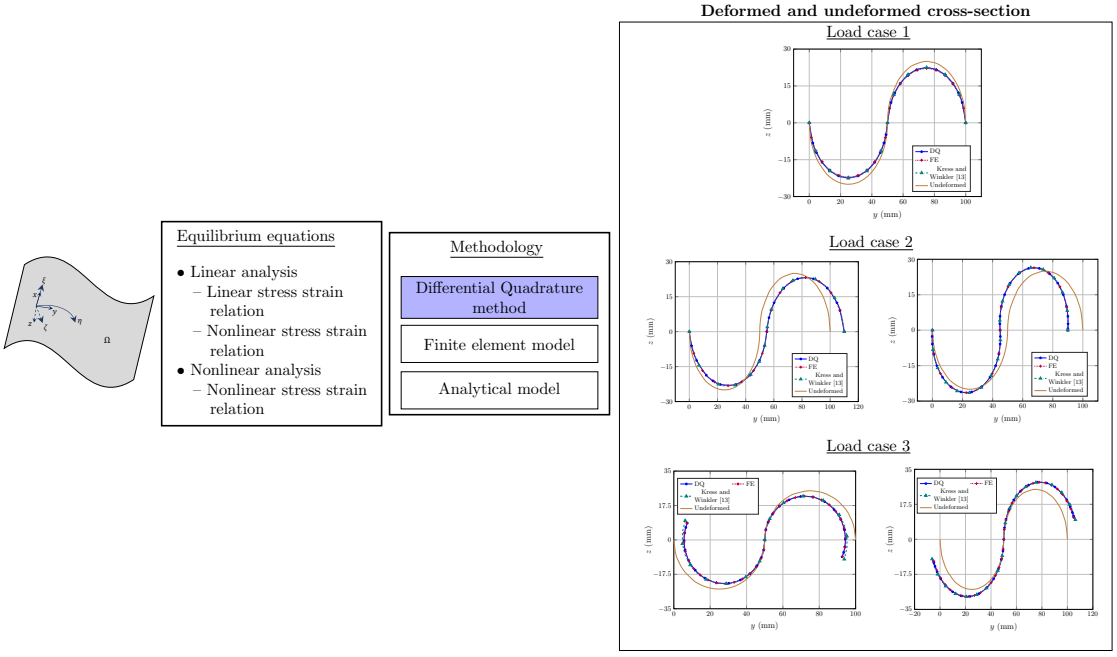
Graphical Abstract

Investigating the nonlinear mechanics of thin corrugated sheets using the differential quadrature method

K. S. Suraj, Fabien Royer*



Highlights

Investigating the nonlinear mechanics of thin corrugated sheets using the differential quadrature method

K. S. Suraj, Fabien Royer*

- The equilibrium equations for a corrugated sheet unit cell are derived using the principle of virtual work following a nonlinear analysis.
- The differential quadrature (DQ) method is employed to solve the nonlinear equilibrium equations for various loading and boundary conditions.
- In the small-strain regime, the DQ accuracy is ascertained by comparison with both an existing analytical model and a fully nonlinear finite element simulation. On the other hand, in the large-strain regime, validation is performed against the fully nonlinear finite element model.
- Detailed study investigates additional terms arising from nonlinear analysis in the Euler-Lagrange equations of a thin, singly curved, corrugated sheet.

Investigating the nonlinear mechanics of thin corrugated sheets using the differential quadrature method

K. S. Suraj[a], Fabien Royer*[a]

[a]*Sibley School of Mechanical and Aerospace Engineering, Cornell University, Ithaca, 14850, NY, USA*

Abstract

Corrugation sheets are extensively used as lightweight engineering structures with a highly anisotropic behavior, as they provide stability under buckling loads and effective energy absorption capabilities. Thus, understanding their geometrically nonlinear response is essential in applications involving large deformations. However, the nonlinear analysis of corrugated sheets is complicated, making it challenging to derive analytical solutions. In the present study, the nonlinear equilibrium equations are derived using the principle of virtual work, following the Green-Lagrange strain and linear curvature displacement derivative approximations, for a globally flat, thin, circular corrugated sheet. Owing to its simplicity, the differential quadrature (DQ) method is well known for its high accuracy and ease of implementation for solving differential equations. Therefore, the nonlinear equilibrium equations of a circular corrugated sheet are solved incrementally using the DQ method, adopting nonuniform grid points for various loading and boundary conditions. A convergence study is conducted to determine the optimal number of grid points required to accurately predict the deformed shape. The accuracy of the DQ method in the small deformation regime is ascertained by comparing the solutions with the existing analytical result. Moreover, full nonlinear finite element analyses are performed to verify the DQ results for both small and large deformation regimes for all the load cases. In addition, a comparison study is performed to investigate the effect of additional terms in the

*Corresponding author

Email address: fabienr@cornell.edu (Fabien Royer*)

equilibrium equations arising from nonlinear analysis, in contrast to those obtained from linear analysis. Finally, the present model is further extended to predict the deformation of a complex corrugated profile, demonstrating its applicability over a broad range of geometries.

Keywords: Corrugated sheet, Nonlinear analysis, Equilibrium equations, Differential quadrature method, Finite element analysis

---

1. Introduction

Corrugated structures have been widely used in engineering applications due to their special characteristics, such as anisotropic behavior, high stiffness-to-weight ratio, enhanced buckling resistance, and energy absorption capabilities. The engineering application of corrugated structures includes beams with corrugated web, corrugated tunnels and pipes, marine structures, rocket fuel storage tanks, oil and gas transmission pipelines, ships, corrugated bulkhead [1, 2, 3, 4, 5, 6, 7]. Corrugated structures are also well known for their multifunctional characteristics. Norman et al. [8] introduced an innovative multistable behavior with a corrugated sheet. The multistability arose from the interaction between internal prestress and nonlinear geometrical changes during deformation. These authors further introduced curvature along the corrugation profile [9]. This allowed the material to undergo significant elastic changes without localized stretching of its surface. These structures hold potential for morphing applications, providing both structural integrity and the capacity for substantial shape transformations.

Analyzing corrugated plates typically involves two primary approaches. The first is a high fidelity analysis, where the full corrugated plates are modeled as fully resolved shell structures. This approach is accurate, but the analyses are either limited to the linear regime or computationally challenging due to the inherent nonlinearity. Many researchers have investigated simplified models to capture the fundamental mechanical behavior of corrugated sheets. For instance, Yokozeki et al. [10] proposed a simple analytical model to evaluate the initial bending stiffness of corrugated composites in both the longitudinal and transverse directions. The approach involves using Castigliano's theorem to calculate the global deflection or rotation, which is then used to derive the transverse modulus. The model's predictions show good agreement with the experimental results. A closed-form solution based

on the Mindlin–Reissner plate theory was developed by Chang et al. [11] to describe the linear flexural behavior of corrugated core sandwich plates for various boundary conditions. Subsequently, Thill et al. [12] performed a numerical analysis to study the complete three-stage tensile behavior of trapezoidal corrugated laminates with local elasto–plastic material definitions. Kress and Winkler [13] derived the closed-form solution for a globally flat thin circular corrugated sheet by solving the equilibrium equations in the linear regime for various load cases. The results agreed well with the linear finite element (FE) solution. Thurnherr et al. [14] proposed a numerical model consisting of rods and discrete torsional springs to analyze the governing mechanisms that drive the nonlinear tensile behavior. The model was validated through comparison with a nonlinear finite element analysis and further confirmed experimentally using 3D-printed samples.

An alternative approach involves simplified analyses, wherein the corrugated plates are idealized as orthotropic plates with equivalent mechanical properties. Using this method, McFarland [15] investigated the equivalent flexural rigidity of rectangular corrugated plates. Subsequently, Briassoulis [16] derived equivalent orthotropic properties for thin sinusoidal corrugated shells using Castigliano's second theorem. The resulting stiffness parameters were then compared with existing expressions [17], and improved formulations were proposed. Dayyani et al. [18] presented numerical and analytical methods for modeling composite corrugated cores subjected to tensile and three-point bending loads. Later, a geometric nonlinear analysis of a trapezoidal corrugated sheet was reported by Samanta and Mukhopadhyay [19], where an equivalent orthotropic model was proposed to account for both extensional and bending rigidities. Further, the analysis was extended to compute the free vibration characteristics of the corrugated sheet. Xi et al. [20] proposed a homogenization-based analytical model for generalized corrugated shapes based on the simplified geometry of a unit cell and the stiffness properties of the original sheet. The proposed model was validated with the existing model and FE analysis for two numerical examples. A mesh-free Galerkin approach was used by Peng et al. [21] to investigate the equivalent elastic properties of sinusoidal and trapezoidal corrugated plates. Later, this approach was adopted by Liew et al. [22] for a geometric nonlinear analysis of stiffened and unstiffened corrugated plates based on the first-order shear deformation theory. Isogeometric analysis (IGA) for free and forced vibration of sinusoidally corrugated is proposed by Mohammadi

Hassan et al. [23]. A detailed comparison study is performed to demonstrate the validity and efficiency of the proposed method. The numerical results demonstrate that the IGA can provide accurate results due to the capability of precisely approximating any segments of the corrugation. Further, this method is extended to study the free vibration of trapezoidally corrugated nanocomposite laminated panels with the considering of corrugation effect [24].

Despite their widespread applications, the nonlinear theoretical modeling of corrugated shells remains a significant challenge [6]. Most analytical models in the literature are confined to the linear regime [19, 21]. However, the complexity arises primarily from the interaction between the geometric nonlinearity and the corrugation geometry, which results in coupled deformation modes. This nonlinear behavior featuring large displacements and rotations, makes the classical linear theories inadequate. As a result, the nonlinear analysis of corrugated sheets is particularly complicated, and obtaining an exact analytical solution is often infeasible. Consequently, developing efficient numerical approaches becomes essential for capturing the fully nonlinear response of such systems. Most commonly, the numerical technique to solve the nonlinear response of corrugated shells is the FE method [25, 26, 27, 28] despite its dependency on element type and meshes, along with the disadvantage of being time-consuming.

The differential quadrature (DQ) method has proven to be a powerful and efficient numerical technique for solving nonlinear differential equations, particularly in problems involving large gradients and complex boundary conditions [29, 30, 31, 32]. Its discretizations and programming procedures are straightforward, making it the tool of choice for many researchers for a broad range of engineering problems. Its advantage lies in approximating derivatives at discrete points using weighted linear sums, allowing accurate results with relatively few grid points [33, 34]. The method has proven to be an efficient numerical technique for solving differential equations in various structural mechanics problems, including beams, plates, and shells [35, 36, 37, 38, 39]. It has also been further extended to solve various mechanics problems involving nonlinear differential equations as well [40, 41, 42]. Ng et al. [43] successfully used the generalized differential quadrature (GDQ) method to investigate the stability of a conical shell. This method was extended to the free vibration analysis of truncated conical panels [44] and

rotating composite laminated conical shells [45]. Additionally, the GDQ method has been successfully applied to thick composite laminates and 3D problems with the layer-wise modeling technique [46, 47, 48].

The present study introduces a comprehensive nonlinear formulation for thin, singly curved corrugated shells by deriving the governing differential equations using the principle of virtual work with Green–Lagrange strain and linear curvature kinematics. Unlike previous works limited to linear or simplified nonlinear models, this study applies the differential quadrature method to solve the fully nonlinear governing equations for corrugated shells under various loading and boundary conditions. The study further examines the effect of coupling the linear equilibrium equations with nonlinear stress resultants, demonstrating that this formulation enables accurate deformation predictions over a wide range of load cases, even in the large deformation regime. In addition, the analysis of circular corrugated sheets is also performed using a fully nonlinear finite element model for given loading and boundary conditions. The DQ and FE models are validated with the existing analytical solution for small deformations. Following validation, these models are extended to predict the deformation of the corrugated shell for cases involving large deformations. The study examines three distinct loading conditions. Two involve applying displacements in the x or ξ and y directions, while the other applies curvatures about the x or ξ axis. For each load case, the DQ method accurately predicts the deformed configuration even in the large deformation regime. The results highlight the importance of using Green–Lagrange strain over linear strain formulations for improved accuracy in nonlinear analyses. Once the validation is ascertained for a simple geometry, the present model is extended to predict the deformed shape of a complex corrugation profile in all three load cases discussed above.

The article is divided into nine sections. Section 2 explains the geometry of the circular corrugated sheet. Section 3 provides an in-depth discussion of kinematics, equilibrium and constitutive equations of a thin circular corrugated shell. The DQ method employed to solve the nonlinear differential equations is discussed in Section 4. Section 5 discusses the nonlinear FE model, and the numerical results for various loading conditions and discussions are presented in Section 6. A comparison study between the equilibrium equations obtained from linear and nonlinear analyses is performed in Section 7. The results corresponding to a complex corrugation profile are shown

in Section 8. Finally, concluding remarks can be found in Section 9.

2. Geometric properties of the corrugated sheet

This section presents the geometry of the circular corrugated sheet under consideration. The local curvilinear coordinate system, ξ, η, and ζ, is defined over a single curved shell corrugation such that the local coordinate ξ is parallel to the global x axis. As shown in Figure 1, at any point, the local coordinates η and ζ are tangential and normal to the corrugated sheet, respectively. The figure illustrates a unit cell of radius R, expanded over the domain Ω. λ and Λ are the material corrugation wavelength and corrugation wavelength mapped onto the shell's mid-surface. A is the corrugation amplitude and $2\phi_0$ is the angle subtended by the corrugation (half unit cell). The geometric parameters are related by the following equations:

$$A = R(1 - \cos\phi_0), \qquad \Lambda = 4\,R\sin\phi_0, \qquad \lambda = 4\,R\phi_0 \tag{1}$$

Considering a piecewise circular corrugation shape gives the absolute value of the curvature $|\kappa| = 1/R$, where R is defined as a positive quantity. However, the curvature κ changes sign between the first and second half of the unit cell. Thus, the curvature and radius are related by an additional parameter m such that:

$$\kappa = \frac{m}{R} \tag{2}$$

where m takes the value +1 in the first half and -1 in the second half of the unit cell. Hence, the coordinated of any points on the corrugated sheet are given by:

$$\begin{aligned} x &= \xi \\ y &= R\,[S + (2 - m)\sin\phi_0] \\ z &= -m[RC - (R - A)] \end{aligned} \tag{3}$$

where,

$$\begin{aligned} S &= \sin\left(\frac{\eta}{R} - (2 - m)\phi_0\right) \\ C &= \cos\left(\frac{\eta}{R} - (2 - m)\phi_0\right) \end{aligned} \tag{4}$$

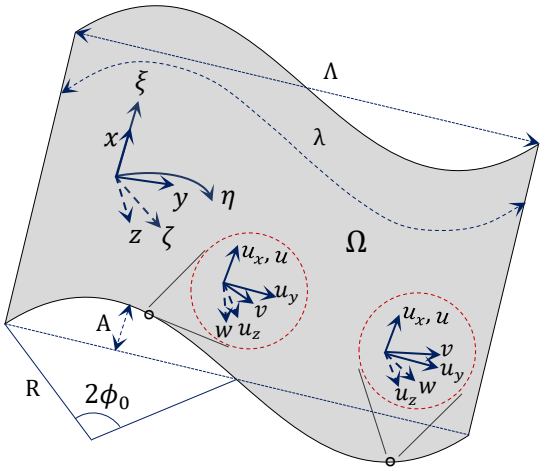


Figure 1: Geometry of a circular corrugated unit cell.

As illustrated in Figure 1, the displacements along the Cartesian coordinate system are defined as u_x, u_y and u_z, while in the curvilinear coordinate system, they are represented as u, v and w. The displacement transformation between these two coordinate systems can be performed by:

$$\begin{bmatrix} u_x \\ u_y \\ u_z \end{bmatrix} = \begin{bmatrix} 1 & 0 & 0 \\ 0 & C & -mS \\ 0 & mS & C \end{bmatrix} \begin{bmatrix} u \\ v \\ w \end{bmatrix} \tag{5}$$

3. Governing equations

3.1. Classical plate kinematics

Let $\overline{U}$ be the displacement vector, where components u, v, and w are functions of ξ, η, and ζ in an orthogonal curvilinear coordinate system (ξ, η, ζ). Consistent with the assumptions of Classical Plate Lamination Theory (CPLT), the components of the displacement vector are defined as follows:

$$\begin{aligned} u(\xi,\eta,\zeta) &= u^0(\xi,\eta) - \zeta\frac{\partial w}{\partial \xi} \\ v(\xi,\eta,\zeta) &= v^0(\xi,\eta) - \zeta\frac{\partial w}{\partial \eta} \\ w(\xi,\eta,\zeta) &= w^0(\xi,\eta) \end{aligned} \tag{6}$$

where the subscript 0 denotes the displacements of a point $(\xi, \eta, 0)$ on the shell mid-plane.

The total strain $\boldsymbol{\varepsilon}$ can be decomposed into membrane strain $\boldsymbol{\varepsilon}^0$ and flexural strain $\boldsymbol{\varepsilon}^1$ such that:

$$\boldsymbol{\varepsilon} = \boldsymbol{\varepsilon}^0 + \zeta\, \boldsymbol{\varepsilon}^1 \tag{7}$$

The membrane strain is decomposed into normal strain ε^0_{ii} where $i = 1, 2$, and shear strain γ^0_{12}. These components are computed using the Green-Lagrange strain tensor in curvilinear coordinate system, and are given by [49]:

$$\begin{aligned}
\varepsilon^0_{11} &= \frac{\partial u^0}{\partial \xi} + \frac{1}{2}\left[\left(\frac{\partial u^0}{\partial \xi}\right)^2 + \left(\frac{\partial v^0}{\partial \xi}\right)^2 + \left(\frac{\partial w^0}{\partial \xi}\right)^2\right] \\
\varepsilon^0_{22} &= \frac{\partial v^0}{\partial \eta} - \kappa\, w^0 + \frac{1}{2}\left[\left(\frac{\partial u^0}{\partial \eta}\right)^2 + \left(\frac{\partial v^0}{\partial \eta} - \kappa\, w^0\right)^2 + \left(\frac{\partial w^0}{\partial \eta} + \kappa\, v^0\right)^2\right] \\
\gamma^0_{12} &= \frac{\partial v^0}{\partial \xi} + \frac{\partial u^0}{\partial \eta} + \left[\frac{\partial u^0}{\partial \xi}\frac{\partial u^0}{\partial \eta} + \frac{\partial v^0}{\partial \xi}\left(\frac{\partial v^0}{\partial \eta} - \kappa\, w^0\right) + \frac{\partial w^0}{\partial \xi}\left(\frac{\partial w^0}{\partial \eta} + \kappa\, v^0\right)\right]
\end{aligned} \tag{8}$$

The bending strain corresponds to the change in curvature of classical plate undergoing moderate rotation, which is a linear function of the displacement derivatives, and is given by [49]:

$$\begin{aligned}
\varepsilon^1_{11} &= -\frac{\partial^2 w^0}{\partial \xi^2} \\
\varepsilon^1_{22} &= -\frac{\partial^2 w^0}{\partial \eta^2} - \kappa \frac{\partial v^0}{\partial \eta} \\
\varepsilon^1_{12} &= -2\frac{\partial^2 w^0}{\partial \xi \partial \eta} - \frac{3}{2}\kappa \frac{\partial v^0}{\partial \xi} + \frac{1}{2}\kappa \frac{\partial u^0}{\partial \eta}
\end{aligned} \tag{9}$$

Note that higher order displacement derivatives need to be included in the curvature when the corrugated sheet undergoes large rotations.

3.2. Equations of motion for a thin circular corrugated sheet

The equations of motion for a thin circular corrugated sheet following CPLT are derived using the principle of virtual work. The static version of the principle of virtual work is [49]:

$$\delta\, \Pi = \delta\, (U + V) = 0 \tag{10}$$

where U is the strain energy, and V is the external work. Based on a prescribed displacement (Eq.6) and strain field (Eq.8), the virtual strain energy can be expressed as:

$$\begin{aligned}
\delta U &= \int_{\Omega} \Big\{ \int_{-\frac{h}{2}}^{\frac{h}{2}} \sigma_{ij}\, \delta\, \varepsilon_{ij}\ d\zeta \Big\}\, d\xi\, d\eta \\
&= \int_{\Omega} \Big\{ \int_{-\frac{h}{2}}^{\frac{h}{2}} \sigma_{ij}\, \delta\, (\varepsilon^0_{ij} + \zeta\, \varepsilon^1_{ij})\ d\zeta \Big\}\, d\xi\, d\eta \\
&= \int_{\Omega} \Big(N_{11}\, \delta\varepsilon^0_{11} + M_{11}\, \delta\varepsilon^1_{11} + N_{22}\, \delta\varepsilon^0_{22} + M_{22}\, \delta\varepsilon^1_{22} + N_{12}\, \delta\gamma^0_{12} \\
&\qquad + M_{12}\, \delta\varepsilon^1_{12} \Big) d\xi\, d\eta
\end{aligned} \tag{11}$$

where $\mathbf{N}$ and $\mathbf{M}$ are stress resultants, and h is the thickness of corrugated sheet. Assuming p_1, p_2 and q are external distributed loads, then the virtual external work is written as:

$$\delta V = \int_{\Omega} \left(p_1\, \delta\, u^0 + p_2\, \delta\, v^0 + q\, \delta\, w^0 \right)\, d\xi\, d\eta \tag{12}$$

The Euler-Lagrange equations, or the equations of motion of a thin circular corrugated sheet, derived from the principle of virtual work, depend upon the choice of strain and curvature assumed above. In the present study, the equilibrium equations are derived using the Green-Lagrange strain and the assumption of a linear curvature displacement derivatives relationship. The equations are derived by substituting equations 11 and 12 into equation 10, followed by an integration by parts to relieve the virtual displacements $(\delta u^0, \delta v^0, \delta w^0)$ in Ω. The Euler-Lagrange equations are obtained by setting the coefficients of δu^0, δv^0, and δw^0 in Ω to zero separately:

$$\begin{cases}
\delta u^0\text{:} & \dfrac{\partial N_{11}}{\partial \xi} + \dfrac{\partial N_{12}}{\partial \eta} + \dfrac{\kappa}{2}\dfrac{\partial M_{12}}{\partial \eta} + \mathcal{N}(u^0, v^0, w^0) + p_1 = 0 \\
\delta v^0\text{:} & \dfrac{\partial N_{12}}{\partial \xi} + \dfrac{\partial N_{22}}{\partial \eta} - \dfrac{3\kappa}{2}\dfrac{\partial M_{12}}{\partial \xi} - \kappa\dfrac{\partial M_{22}}{\partial \eta} + \mathcal{O}(u^0, v^0, w^0) + p_2 = 0 \\
\delta w^0\text{:} & \dfrac{\partial^2 M_{11}}{\partial \xi^2} + 2\dfrac{\partial^2 M_{12}}{\partial \xi \partial \eta} + \dfrac{\partial^2 M_{22}}{\partial \eta^2} + \kappa N_{22} + \mathcal{P}(u^0, v^0, w^0) + q = 0
\end{cases} \tag{13}$$

where,

$$\mathcal{N}(u^0, v^0, w^0) = \frac{\partial}{\partial \xi}\left(N_{11}\frac{\partial u^0}{\partial \xi} + N_{12}\frac{\partial u^0}{\partial \eta} \right) + \frac{\partial}{\partial \eta}\left(N_{12}\frac{\partial u^0}{\partial \xi} + N_{22}\frac{\partial u^0}{\partial \eta} \right)$$

$$\mathcal{O}(u^0,v^0,w^0)=\frac{\partial}{\partial\xi}\left(N_{11}\frac{\partial v^0}{\partial\xi}+N_{12}\left\{\frac{\partial v^0}{\partial\eta}-\kappa\, w^0\right\}\right)+\frac{\partial}{\partial\eta}\left(N_{12}\frac{\partial v^0}{\partial\xi}+\right.$$
$$\left.N_{22}\left\{\frac{\partial v^0}{\partial\eta}-\kappa\, w^0\right\}\right)+\kappa\left(N_{12}\frac{\partial w^0}{\partial\xi}+N_{22}\left\{\frac{\partial w^0}{\partial\eta}+\kappa\, v^0\right\}\right)$$
$$\mathcal{P}(u^0,v^0,w^0)=\frac{\partial}{\partial\xi}\left(N_{11}\frac{\partial w^0}{\partial\xi}+N_{12}\left\{\frac{\partial w^0}{\partial\eta}+\kappa\, v^0\right\}\right)+\frac{\partial}{\partial\eta}\left(N_{12}\frac{\partial w^0}{\partial\xi}+\right.$$
$$\left.N_{22}\left\{\frac{\partial w^0}{\partial\eta}+\kappa\, v^0\right\}\right)+\kappa\left(N_{12}\frac{\partial v^0}{\partial\xi}+N_{22}\left\{\frac{\partial v^0}{\partial\eta}-\kappa\, w^0\right\}\right) \quad (14)$$

The additional terms $\mathcal{N}$, $\mathcal{O}$, and $\mathcal{P}$ arise from the nonlinear strain assumption and have been thoroughly examined in Section 7 for various loading conditions. From Section 7, it is evident that solving the equilibrium equations derived from the linear strain analysis and computing the stress resultants using the nonlinear Green-Lagrange strain is sufficient to predict the deformed shape of the corrugated sheet across all load cases, even at sufficiently large applied strain and curvatures. Consequently, these terms are omitted in the rest of the paper (except Section 7) to reduce the computational expense for all load cases.

3.3. Constitutive equation

For a thin laminated shell, the constitutive equations are given by [50]:

$$\begin{bmatrix}\boldsymbol{N}\\ \boldsymbol{M}\end{bmatrix}=\begin{bmatrix}\boldsymbol{A} & \boldsymbol{B}\\ \boldsymbol{B} & \boldsymbol{D}\end{bmatrix}\begin{bmatrix}\boldsymbol{\varepsilon}^0\\ \boldsymbol{\varepsilon}^1\end{bmatrix} \quad (15)$$

with,

$$\boldsymbol{\varepsilon}^0=\begin{Bmatrix}\varepsilon^0_{11}\\ \varepsilon^0_{22}\\ \gamma^0_{12}\end{Bmatrix},\qquad \text{and}\qquad \boldsymbol{\varepsilon}^1=\begin{Bmatrix}\varepsilon^1_{11}\\ \varepsilon^1_{22}\\ \varepsilon^1_{12}\end{Bmatrix} \quad (16)$$

where the strain and curvature have been defined in equations 8 and 9, respectively. **A**, **B**, and **D** are the in-plane, coupling, and bending matrices of the laminate, and are written as:

$$[A_{ij},B_{ij},D_{ij}]=\int_{-h/2}^{h/2}\bar{Q}_{ij}\left[1,z,z^2\right]\mathrm{d}z=\sum_{k=1}^{n}\int_{z_k}^{z_{k+1}}\bar{Q}^{(k)}_{ij}\left[1,z,z^2\right]\mathrm{d}z \quad (17)$$

where $\bar{Q}^{(k)}_{ij}$ represents the in-plane material stiffness constant of an individual ply at location z through the thickness of the laminate, transformed to

the laminate's coordinate system [50], n is the number of lamina, and h is the thickness of the laminate. Thus, the equilibrium equations (Eq.13) can be written in terms of material constants and kinematic variables using constitutive and kinematics relations (see Appendix A).

4. Differential quadrature method and solution procedures

The differential quadrature method is employed to solve the nonlinear differential equations with appropriate boundary conditions for various load cases [51]. However, since the method only computes the independent variables at the grid points, difficulties arise while applying multiple boundary conditions involving higher-order terms. To overcome this, various methods are available in the literature. The most commonly used method is the δ *Approach* [30, 52], in which the grid points immediately adjacent to the boundaries are placed in close vicinity to the boundary grid points to define additional boundary conditions. The closeness between the neighboring points is often chosen to be of the order $\delta \sim 10^{-5}$ (distance between grid points normalized by the grid width) [34]. Another commonly used method is the so-called *Built-in method* [52, 53], in which additional boundary conditions are satisfied while calculating the higher order weighting coefficient matrices [33]. However, the *Built-in method* cannot be used for all the boundary conditions in a two-dimensional problem. Considering the complex boundary conditions of a circular corrugated sheet, the δ *Approach* is chosen in the present study, as it is easy to implement. Figure 2 outlines the stepwise implementation of the differential quadrature method for the analysis of a corrugated unit cell for all load cases.

A brief description of the DQ method is discussed next. The essence of the DQ method lies in approximating a function's derivative as a weighted sum of its values across all grid points. Considering a one-dimensional continuously differentiable function $f(\xi)$, the derivative at any grid point can be expressed as [54, 55]:

$$\left[\frac{d\,f(\xi)}{d\xi}\right]_{\xi=\xi_i} = \sum_{j=1}^{N} A_{ij}^{(\xi)}\, f(\xi_j), \qquad i = 1, 2, ..., N \tag{18}$$

where N is the number of grid points and $A_{ij}^{(\xi)}$ is the weighting coefficients of the first order derivative with respect to ξ. Similarly, the higher-order derivatives can be expressed as a linear function of the weight coefficient

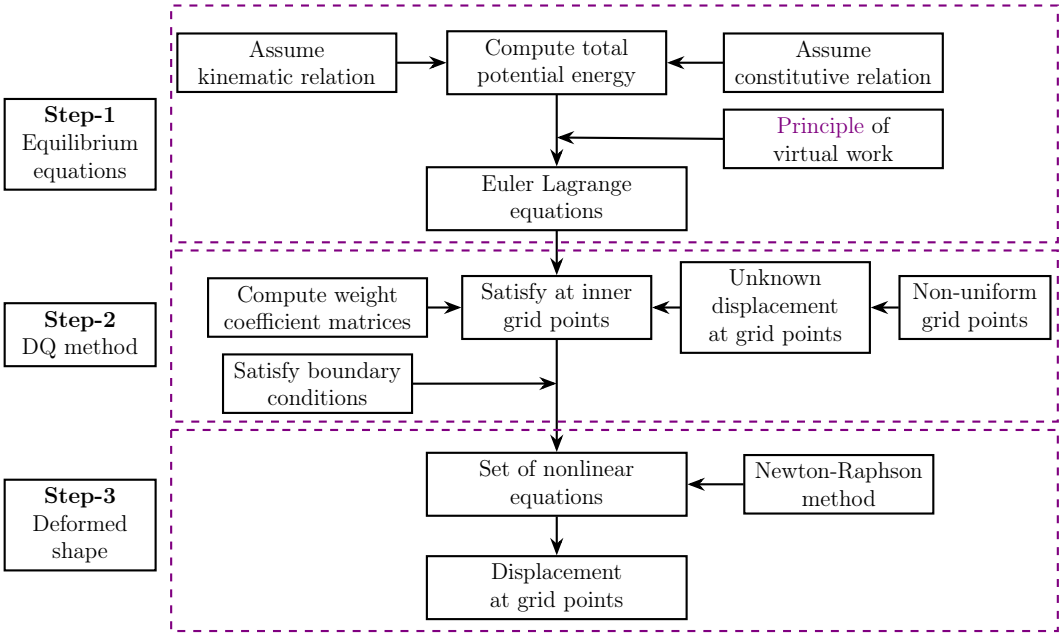


Figure 2: Flowchart of proposed methodology for the analysis of the corrugated sheet.

matrix and the function value at grid points. The weighting coefficients can be computed explicitly as [56]:

$$A_{ij}^{(\xi)} = \frac{\omega'_N(\xi_i)}{(\xi_i - \xi_j)\,\omega'_N(\xi_j)} \qquad (i \neq j), \qquad A_{ii}^{(\xi)} = \sum_{j=1, i\neq j}^{N} \frac{1}{\xi_i - \xi_j} \tag{19}$$

where $\omega(\xi)$ is the Lagrange interpolation function defined as:

$$\begin{aligned} &\omega_N(\xi) = (\xi - \xi_1)(\xi - \xi_2)....(\xi - \xi_i)....(\xi - \xi_{N-1})(\xi - \xi_N), \\ &\omega'_N(\xi_i) = (\xi - \xi_1)(\xi - \xi_2).....(\xi - \xi_{N-1})(\xi - \xi_N) \end{aligned} \tag{20}$$

The weight coefficient for higher order matrices can be computed by explicit formula [56] or using the recursive formulae below:

$$\begin{aligned} &B_{ij}^{(\xi)} = \sum_{k=1}^{N} A_{ik}^{(\xi)} A_{kj}^{(\xi)}, \qquad C_{ij}^{(\xi)} = \sum_{k=1}^{N} B_{ik}^{(\xi)} A_{kj}^{(\xi)}, \qquad D_{ij}^{(\xi)} = \sum_{k=1}^{N} B_{ik}^{(\xi)} B_{kj}^{(\xi)} \\ &(i, j = 1, 2, ..., N) \end{aligned} \tag{21}$$

where $B_{ij}^{(\xi)}$, $C_{ij}^{(\xi)}$ and $D_{ij}^{(\xi)}$ are the weighting coefficients of the second, third and fourth-order derivatives with respect to ξ, respectively. In general, com-

puting the higher-order weighting coefficients explicitly is more accurate and computationally inexpensive than using the recursive formulae, but for a small number of grids, the matrix multiplication approach leads to less computational time and accurate weighting coefficients since the matrix is of a small size [33]. Thus, the recursive formulae are used in the present study as they are convenient to program and stable.

The accuracy of the DQ solution is highly sensitive to the distribution of grid points. For certain classes of problems, a reliable and convergent solution can only be obtained with nonuniformly distributed points [57]. The most popular nonuniform grids are the Chebyshev–Gauss–Lobatto grid distribution, the Gaussian quadrature point distribution and the Gauss–Lobatto –Legendre grid point distribution [58].

In the present study, the translation of corrugated sheets is a two-dimensional continuous differential function. Based on the DQ method, the displacements can be discretized by the following equation:

$$\{\, u^0, v^0, w^0 \,\} \;=\; \sum_{i=1}^{N}\sum_{j=1}^{N} \omega_N(\xi)\,\omega_N(\eta)\,\{u_{ij}^0, v_{ij}^0, w_{ij}^0\} \tag{22}$$

where N is the number of grid points in both ξ and η direction. A Chebyshev–Gauss–Lobatto grid distribution with adjacent δ points is used in the present study for better convergence [34, 58]. Thus, the grid point coordinates in direction ξ and η are defined as:

$$\begin{aligned}
&\xi_1 = 0, \quad \xi_2 = \delta L, \quad \xi_{N-1} = (1-\delta)L, \quad \xi_N = L \\
&\xi_i = (1 - cos[(i-1)\pi/(N-3)])\; L, \qquad (i = 3, 4, .., N-2) \\
&\eta_1 = 0, \quad \eta_2 = \delta\lambda, \quad \eta_{N-1} = (1-\delta)\lambda, \quad \eta_N = \lambda \\
&\eta_j = (1 - cos[(j-1)\pi/(N-3)])\; \lambda \qquad (j = 3, 4, .., N-2)
\end{aligned} \tag{23}$$

where L is the length of the unit cell along the ξ direction and λ is the material corrugation wavelength of the periodic unit cell.

Solving equations 13 on the grid points shown in Figure 3, gives a set of nonlinear equations in the form:

$$[K]\{\overline{U}\} + [F(\overline{U})]\{\overline{U}\} = \overline{P} \tag{24}$$

where the size of both matrix of linear terms $[K]$ and matrix of nonlinear terms $[F(\overline{U})]$ is $3(N-2)^2 \times 3(N-2)^2$, $\overline{U}$ is the vector of unknown displacements at the grid points, and $\overline{P}$ is the load vector.

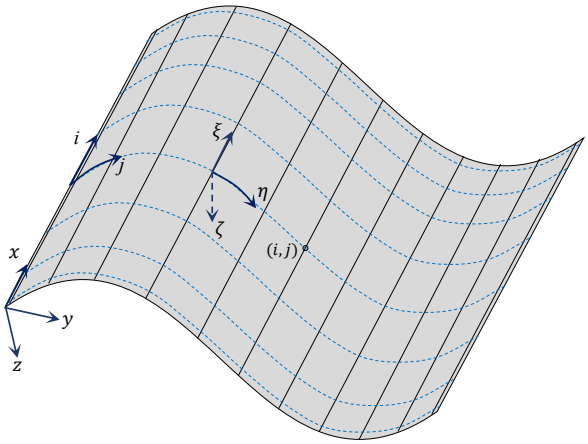


Figure 3: A generalized grid points to solve the governing differential equations 13.

For an $N \times N$ grid, there are a total of $3N^2$ unknowns. Therefore, $3N^2$ independent equations are required to solve for these unknowns. The system of differential equations must be satisfied at the interior grid points, yielding $3(N-2)^2$ equations. The remaining equations are derived from the Dirichlet and Neumann boundary conditions. However, adopting the δ method to satisfy the Neumann boundary conditions slightly altered the number of equations obtained. Nonetheless, the total number of equations and unknowns remains the same.

The Newton-Raphson technique is implemented to solve the set of nonlinear equations (Eq. 24). The prescribed tolerance is set to $10^{-9} - 10^{-8}$. On completion of the Newton-Raphson step, the stability of the solution is ascertained by ensuring that the Jacobian is positive definite. During numerical simulations, it has been observed that initializing the analysis with random guesses often leads to divergence or requires a larger number of iterations for convergence. To achieve faster convergence, the linear part of equation 24 ($[K]\{\overline{U}\} = \overline{P}$) is solved first, and the solution serves as the initial guess for solving the entire set of nonlinear equations.

5. Finite element model

Nonlinear finite element analyses are carried out using the commercially available software ABAQUS [59], and the results are used to validate the DQ solution alongside existing analytical results. S8R5 shell elements (8-node

doubly curved thin shell, reduced integration, five degrees of freedom per node) are used to carry out the FE analyses of the thin corrugated sheet for all loading conditions. The mesh type is chosen from a detailed study conducted for all the load cases. For load case 1 (subsection 6.2), the S4R element type (4-node quadrilateral shell element with reduced integration) tends to predict a stiffer solution compared to the analytical solution [13]. However, for the remaining load cases, it provides sufficiently accurate predictions. To ensure consistency across all analyses, the S8R5 element type has been chosen for all load cases. The analyses are performed using the general static option in ABAQUS. A typical mesh size of 35 elements along the curvilinear coordinate η direction is chosen based on a mesh convergence study, ensuring computational efficiency and accuracy. Figure 4 shows a unit cell over the domain Ω with boundaries Ω_1 and Ω_3 along the ξ direction while Ω_2 and Ω_4 are along the η direction. The prescribed displacement boundary conditions are applied for each load case except for case 3 (subsection 6.4). In load case 3, a pure bending about the ξ direction is applied, with constant curvature. In the FE model, this is simulated by applying an equivalent bending moment on the relevant boundaries, as obtained from equation 15.

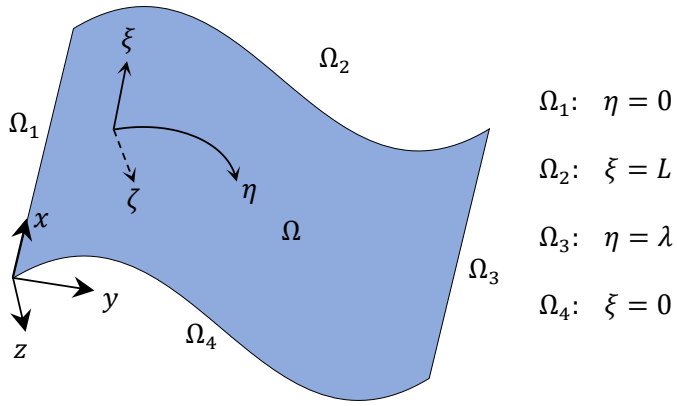


Figure 4: Circular corrugated unit cell simulated in the FE model.

6. Results

This section presents the validation of the DQ model by comparing the solution with existing analytical solution and FE simulation result, for each load cases. As a reminder, Figure 1 illustrates the geometry of the circular

corrugated unit cell. Although the full DQ model includes all the stiffness terms needed to describe the orthotropic laminates, the analyses presented use steel (isotropic) with Young's Modulus $E = 210{,}000$ MPa and Poisson's ratio $\nu = 0.3$ of thickness $h = 1$ mm. Without loss of generality, the two independent parameters describing the corrugated sheet are chosen to be $R = 25$ mm and $\phi_0 = 90°$. The additional geometric parameters are $A = 25$ mm and $\Lambda = 100$ mm, computed using equation 1. The dimension along the ξ direction, only relevant in the FE model and Load case 1, is set to 1000 mm. A more complex profile is then considered in Section 8, where its associated geometric properties are also described.

6.1. Grid convergence study

As pointed out earlier, the DQ solution is sensitive to the number of grid points. Therefore, a systematic convergence study is essential to identify the minimum number of grid points required to predict the sheet's deformed shape accurately. As an illustration, a convergence study with Chebyshev–Gauss–Lobatto grid points is performed to simulate the deformed shape for load case 2 (subsection 6.3). Increasing the number of grid points from 13 to 19 yields a DQ solution that closely aligns with the analytical result, as illustrated in Figure 5. Notably, the number of grid points also includes two additional δ points defined near boundaries to enforce the Neumann boundary conditions.

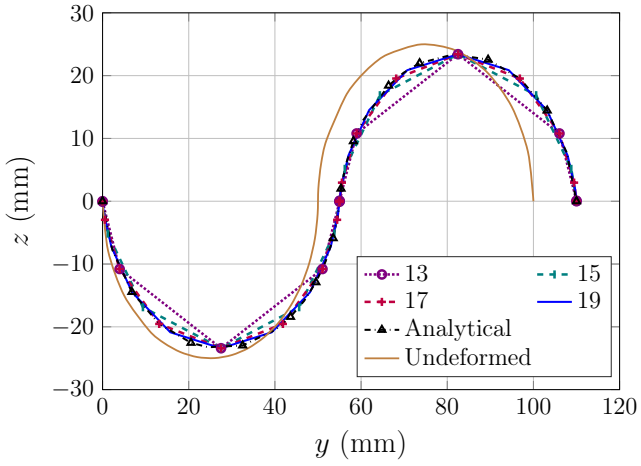


Figure 5: Cross-sectional view of the deformed unit cell with varying grid point numbers.

As can be seen, 15 grid points are sufficient to predict the deformed shape accurately. However, for a smoother shape, one may choose 19 grid points. It should be noted that, in all figures, the analytical results correspond to the solution provided by Kress and Winkler [13].

6.2. Load case 1

In this load case, a uniform engineering strain ϵ_x is applied to the unit cell along boundary Ω_4, while the displacement of boundary Ω_2 is restrained in the ξ direction. In addition, the Ω_1 and Ω_3 boundaries are pinned to prevent any deformation in the y and z directions. The displacement u^0 is a function of the applied engineering strain ϵ_x and does not vary in the η direction. Because of Poisson's ratio of the corrugated sheet, v^0 and w^0 depend on η. Moreover, the displacements v^0 and w^0 remain constant along the ξ direction. Consequently, the derivative of displacement u^0 in the η direction, and the derivative of displacement v^0 and w^0 in the ξ direction, vanish from the governing differential equations (Eq.A.3). However, for verification purpose whole governing differential equations (Eq.A.3) has been considered. The boundary conditions described above, along with the moment-free conditions on Ω_1 and Ω_3 for load case 1, are given as follows:

$$\begin{aligned}
&\Omega_1 : \\
&\quad v^0 = 0, \qquad w^0 = 0, \qquad N_{12} = 0, \qquad M_{22} = 0 \\
&\Omega_2 : \\
&\quad u^0 = 0, \qquad \varphi_1 = 0, \qquad N_{12} = 0 \\
&\Omega_3 : \\
&\quad v^0 = 0, \qquad w^0 = 0, \qquad N_{12} = 0, \qquad M_{22} = 0 \\
&\Omega_4 : \\
&\quad u^0 = \epsilon_x L, \qquad \varphi_1 = 0, \qquad N_{12} = 0
\end{aligned} \tag{25}$$

where, N_{12}, M_{22} are stress resultants. φ_1 is rotation along ξ axis and defined as:

$$\varphi_1 = -\frac{\partial w^0}{\partial \xi} \tag{26}$$

In the DQ analysis, the domain Ω is discretized into $N \times N$ nonuniform grid points given in equation 23. Each grid point is associated with three

equations; hence, a δ point in η direction needs to be defined to satisfy the additional boundary condition. In contrast, boundaries Ω_2 and Ω_4 are associated with only three boundary conditions; therefore, no δ grid point is needed in the ξ direction. The displacement components, u^0, v^0, and w^0, at each grid points are obtained by solving the governing equations (Eq.A.3) and boundary conditions (Eq.25), and are then transformed to obtain the displacements u_x, u_y and u_z, using the transformation rule (Eq.5). These equation are implemented in the commercially available software Python and solved numerically using the Newton-Raphson method. Figure 6 and 7 illustrates the deformed configuration of the corrugated sheet under an axial engineering strains of $\epsilon_x = 0.2$ and 0.5 respectively, predicted by the DQ, FE and existing analytical models. The DQ result is obtained with $N = 19$ grids for a unit cell. For small engineering strain ($\epsilon_x = 0.2$), the DQ result shows excellent agreement with both the analytical [13] and the FE results, as shown in Figure 6. It should be noted that Kress and Winkler [13] derived the analytical solution by solving the linear part of the differential equation (Eq.A.3) for given boundary conditions (Eq.25).

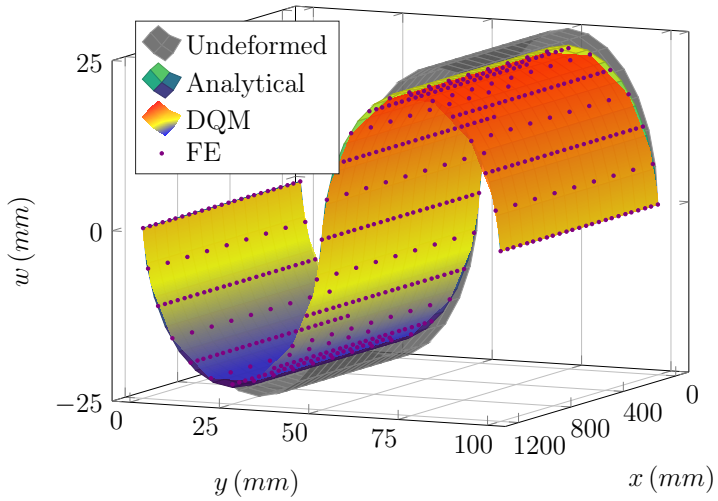


Figure 6: Deformed configuration of a unit cell at engineering strain $\epsilon_x = 0.2$.

The good agreement among the three models confirms the accuracy and derivation involved in the DQ analysis for predicting the deformation response under small strains. It should be noted that only a positive value of ϵ_x is considered due to the possibility of buckling under compression, which has not been considered in the present study. For a moderate strain case

($\epsilon_x = 0.5$), depicted in Figure 7, a noticeable discrepancy is observed between the analytical solution and those predicted by the DQ and FE models. This discrepancy arises from the inherent limitations of the analytical model, which is derived from the underlying assumption of linear strain and is thus valid only for small deformations. In contrast, the DQ model incorporates the Green-Lagrange strain measure to capture large displacements, enabling it to accurately capture the large deformation behavior. The strong agreement between the DQ and FE results in this regime further validates the robustness of the developed DQ model in solving the nonlinear governing differential equations, even in the moderate strain regime.

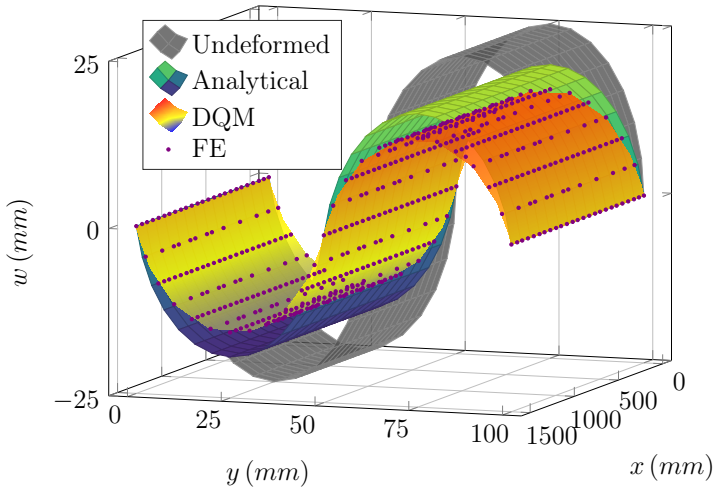


Figure 7: Deformed configuration of a unit cell at engineering strain $\epsilon_x = 0.5$.

Following the validation, both at small and moderate strain, the applied engineering strain (ϵ_x) is further increased until Poisson's effect causes the corrugated sheet to nearly flatten. Figure 8 and 9 demonstrate the deformed shape of the corrugated sheet under higher applied engineering strains, $\epsilon_x = 0.7$ and 0.725, respectively. For better comparison, the deformed configuration is shown together with the corresponding cross-sectional profiles obtained by the DQ and FE methods in both figures. The DQ predictions closely follow the FE results, demonstrating the accuracy of the DQ model even in the highly nonlinear strain regime. However, the assumption of moderate rotations begins to deviate near $\epsilon_x = 0.725$, where an appreciable difference in predicted deformed shape is observed between the DQ and FE results. In a further investigation, the fully nonlinear equilibrium equa-

tions (Eq.13) are solved (see Section 7), which confirmed that the observed discrepancy arises from the assumption of linearity of the curvature with respect to the displacement derivatives. It is worth noting that such effects become significant only under extreme strain conditions. For applications requiring accurate modeling of large rotations, nonlinear shell theories such as those of Flügge–Lur'e–Byrne or Novozhilov [60, 61] may be employed. However, these approaches come at the expense of considerable complexity and computational cost, whereas the present DQ formulation offers an efficient and sufficiently accurate tool across the practically relevant strain regime. It is also important to note that these higher strain values are considered for the demonstration of the formulation to accurately capture deformation in the large strain regime. However, achieving such strain levels may not be practically feasible.

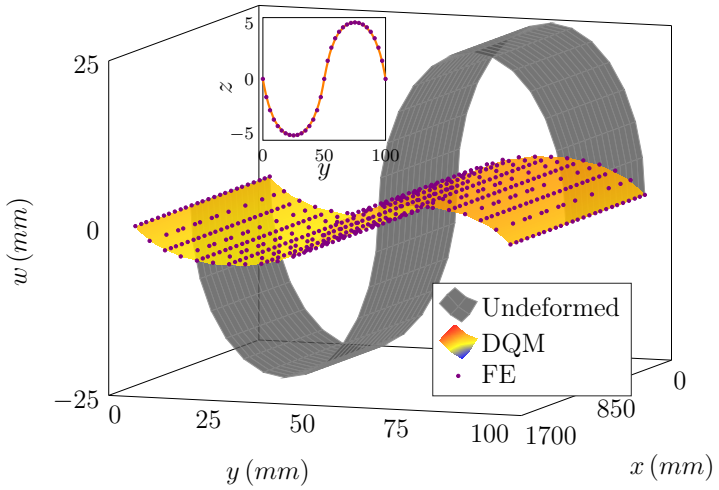


Figure 8: Deformed configuration of the unit cell and associated cross-section at engineering strain $\epsilon_x = 0.7$

In addition to the deformed shape, the true strain components ε^0_{11} and ε^0_{22} obtained from the DQ (using Eq. 8) and those predicted by the FE method are compared as a function of the axial displacement u_x in Figure 10. The axial strain ε^0_{11} increases monotonically and exhibits an excellent match between the two models over the entire displacement range. In contrast, the transverse strain ε^0_{22} becomes increasingly negative with growing axial displacement, reflecting lateral contraction due to Poisson's effect. The close agreement further confirms the robustness and reliability of the DQ

formulation in predicting nonlinear strain behavior under large deformation. It should be noted that load case 1 produces the maximum strain, while the other load cases result in only minor strain levels, therefore, the strain comparison is conducted exclusively for load case 1.

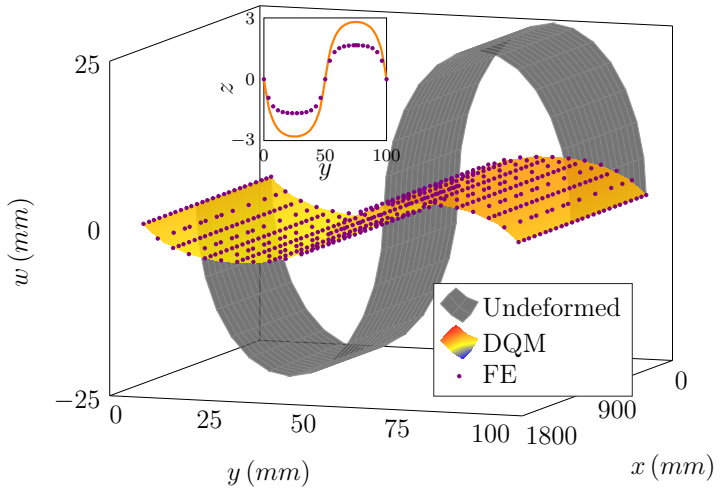


Figure 9: Deformed configuration of the unit cell and associated cross-section at engineering strain $\epsilon_x = 0.725$.

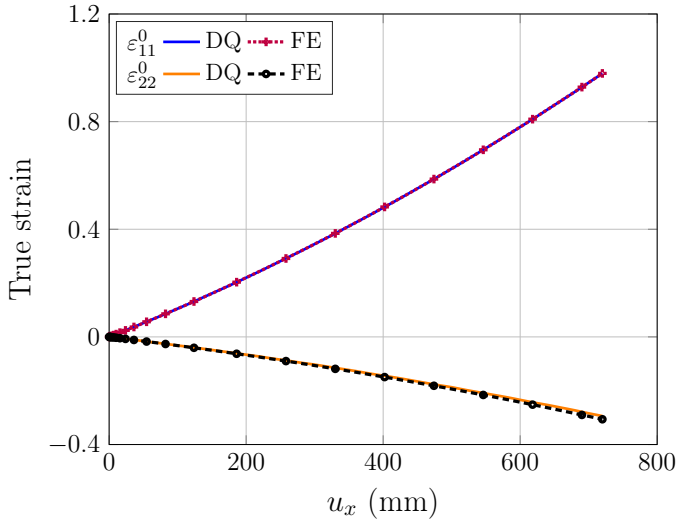


Figure 10: Comparison of true strain prediction using the DQ and FE methods.

6.3. Load case 2

In load case 2, a prescribed displacement $u_y = \epsilon_y \Lambda$ is applied on boundary Ω_3 along the y direction, causing the average strain ϵ_y (normalized by the corrugation wavelength), where ϵ_y can take both positive and negative values. The boundary Ω_1 of the unit cell is pinned to prevent displacements in y and z directions. The displacement components v^0 and w^0 do not vary along the ξ direction; consequently, all the derivatives along the ξ direction are zero. For the given loading and boundary conditions, the displacement u^0 in the ξ direction remains insignificant unless the material undergoes stretching along the y direction, which is deliberately excluded from the scope of the present study. Hence, the governing differential equation for load case 2 simplifies to:

$$
\begin{aligned}
&A_{22}\left[\frac{\partial^2 v^0}{\partial \eta^2} - \kappa\frac{\partial w^0}{\partial \eta} + \left(\frac{\partial v^0}{\partial \eta} - \kappa w^0\right)\left(\frac{\partial^2 v^0}{\partial \eta^2} - \kappa\frac{\partial w^0}{\partial \eta}\right) + \left(\frac{\partial w^0}{\partial \eta} + \kappa v^0\right)\right. \\
&\left.\left(\frac{\partial^2 w^0}{\partial \eta^2} + \kappa\frac{\partial v^0}{\partial \eta}\right)\right] + \kappa D_{22}\left[\frac{\partial^3 w^0}{\partial \eta^3} + \kappa\frac{\partial^2 v^0}{\partial \eta^2}\right] = 0 \\
&\kappa A_{22}\left[\frac{\partial v^0}{\partial \eta} - \kappa w^0 + \frac{1}{2}\left(\frac{\partial v^0}{\partial \eta} - \kappa w^0\right)^2 + \frac{1}{2}\left(\frac{\partial w^0}{\partial \eta} + \kappa v^0\right)^2\right] - \\
&D_{22}\left[\frac{\partial^4 w^0}{\partial \eta^4} + \kappa\frac{\partial^3 v^0}{\partial \eta^3}\right] = 0
\end{aligned}
\tag{27}
$$

The applied displacement, transformed in the local coordinate system, the moment-free boundary conditions at Ω_1 and Ω_3, and the pinned boundary conditions of Ω_1 are written as:

$$
\begin{aligned}
&v^0(\eta = 0) = 0, && v^0(\eta = 4R\phi_0) = \epsilon_y \Lambda \cos\phi_0 \\
&w^0(\eta = 0) = 0, && w^0(\eta = 4R\phi_0) = \epsilon_y \Lambda \sin\phi_0 \\
&\varepsilon_2^1(\eta = 0) = 0, && \varepsilon_2^1(\eta = 4R\phi_0) = 0
\end{aligned}
\tag{28}
$$

The above equations (Eq.27) are only function of η with v^0 and w^0 as variables. Figure 11 depicts the 2D domain in the η direction over which the differential equations (Eq.27) are solved. The domain is discretized in N nonuniform grid points, including two δ points near the boundary. Each grid points are associated with two equations; hence, the δ grid points satisfy the first differential equation together with a curvature boundary condition.

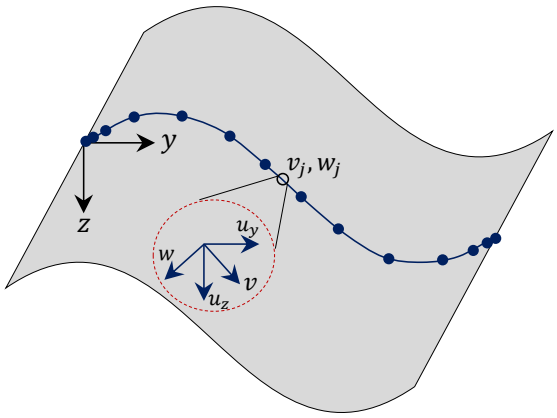


Figure 11: Grid points used to solve the governing differential equations for load case 2.

The governing differential equations in the DQ method take the following form:

$$A_{22}\left[\sum_{k=1}^{N} B_{jk}^{(\eta)} v_k^0 - \kappa_j \sum_{k=1}^{N} A_{jk}^{(\eta)} w_k^0 + \left(\sum_{k=1}^{N} A_{jk}^{(\eta)} v_k^0 - \kappa_j w_j^0\right)\left(\sum_{k=1}^{N} B_{jk}^{(\eta)} v_k^0 - \kappa_j \sum_{k=1}^{N} A_{jk}^{(\eta)} w_k^0\right) + \left(\sum_{k=1}^{N} A_{jk}^{(\eta)} w_k^0 + \kappa_j v_j^0\right)\left(\sum_{k=1}^{N} B_{jk}^{(\eta)} w_k^0 + \kappa_j \sum_{k=1}^{N} A_{jk}^{(\eta)} v_k^0\right)\right] + \kappa_j D_{22}\left[\sum_{k=1}^{N} C_{jk}^{(\eta)} w_k^0 + \kappa_j \sum_{k=1}^{N} B_{jk}^{(\eta)} v_k^0\right] = 0$$

$$\text{for} \qquad (j = 2, 3, ..., N-2, N-1)$$

$$\kappa_j A_{22}\left[\sum_{k=1}^{N} A_{jk}^{(\eta)} v_k^0 - \kappa_j w_j^0 + \frac{1}{2}\left(\sum_{k=1}^{N} A_{jk}^{(\eta)} v_k^0 - \kappa_j w_j^0\right)^2 + \frac{1}{2}\left(\sum_{k=1}^{N} A_{jk}^{(\eta)} w_k^0 + \kappa_j v_j^0\right)^2\right] - D_{22}\left[\sum_{k=1}^{N} D_{jk}^{(\eta)} w_k^0 + \kappa_j \sum_{k=1}^{N} C_{jk}^{(\eta)} v_k^0\right] = 0$$

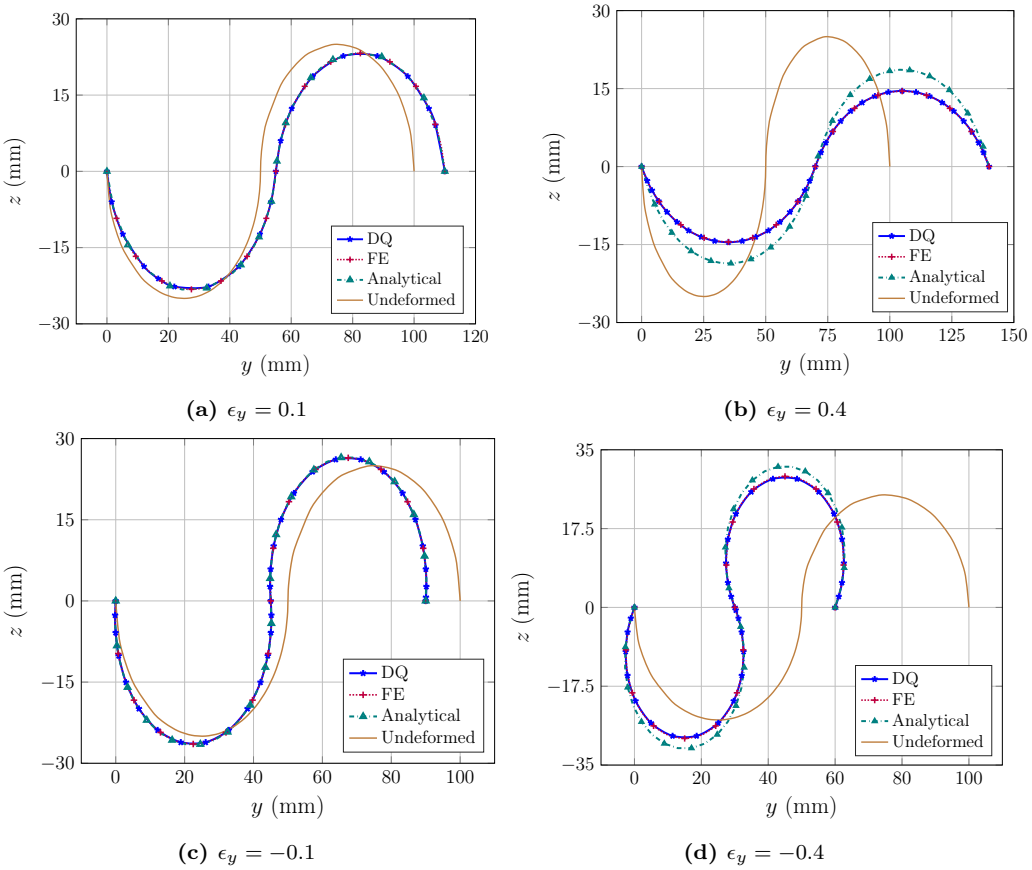
$$\text{for} \qquad (j = 3, 4, ..., N-3, N-2) \tag{29}$$

It is important to note that κ_j in the above equation is positive and negative for the first and second half of the unit cell, respectively. The corresponding

boundary conditions at grid points are expressed as:

$$
\begin{aligned}
&v_1^0 = 0, && v_N^0 = \epsilon_y \Lambda \cos\phi_0 \\
&w_1^0 = 0, && w_N^0 = \epsilon_y \Lambda \sin\phi_0 \\
&\sum_{k=1}^{N} B_{2k}^{(\eta)} w_k^0 + \kappa_2 \sum_{k=1}^{N} A_{2k}^{(\eta)} v_k^0 = 0, && \sum_{k=1}^{N} B_{N-1k}^{(\eta)} w_k^0 + \kappa_{N-1} \sum_{k=1}^{N} A_{N-1k}^{(\eta)} v_k^0 = 0
\end{aligned}
\tag{30}
$$

Figure 12 depicts the deformed cross-section under various in-plane strain levels ϵ_y predicted by different models. A total of 19 grid points are employed in the DQ analysis to obtain a smooth deformed curve. The DQ model results show an excellent agreement with the other two models for small tensile and compressive strains ($\epsilon_y = \pm 0.1$). As the strain level increases to



(a) $\epsilon_y = 0.1$ **(b)** $\epsilon_y = 0.4$

(c) $\epsilon_y = -0.1$ **(d)** $\epsilon_y = -0.4$

Figure 12: Deformed unit cell cross-sections from different models for load case 2.

$\epsilon_y = \pm 0.4$, the deformation becomes notably pronounced, and the influence of geometric nonlinearity is significant. As shown in Figure 12 (b) and 12(d), the nonlinear effects are more prominent under tensile loading than under compressive loading at the same strain level. Despite these nonlinearities, a close correlation is observed between the DQ and FE results, even at higher tensile and compressive strains, thereby ensuring the robustness of the DQ approach in predicting the deformed shape of the corrugated unit cell for load case 2.

Upon validation, the applied strain is further increased, and the deformed cross-section shape is plotted for selected strain levels in both compression and tension. Under tensile loading, the applied strain is increased until the corrugation flattens. Once the corrugation flattened, further increasing the strain violates the assumption of insignificance of u^0 due to Poisson's effect. As a result, the governing equations and boundary conditions for load case 2 must be modified accordingly. Figure 13 depicts the deformed cross-section corresponding to $\epsilon_y = 0.5$ and 0.57. The corrugated sheet becomes almost flat upon applying a displacement equivalent to 0.57 times the corrugation wavelength Λ along the boundary Ω_3 in the y direction. The results obtained from the DQ model with the Green-Lagrange strain formulation match well with those obtained from the FE simulation.

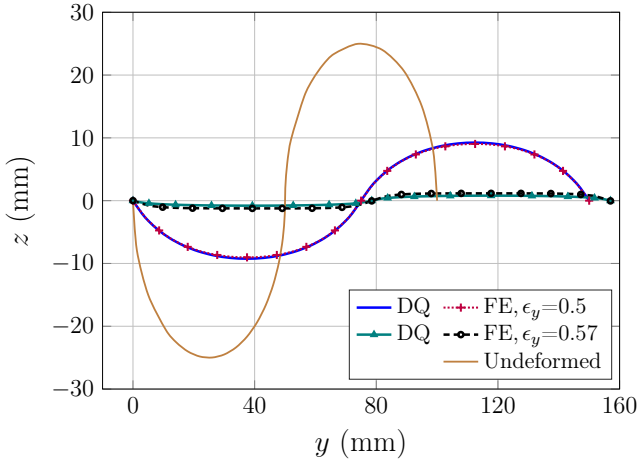
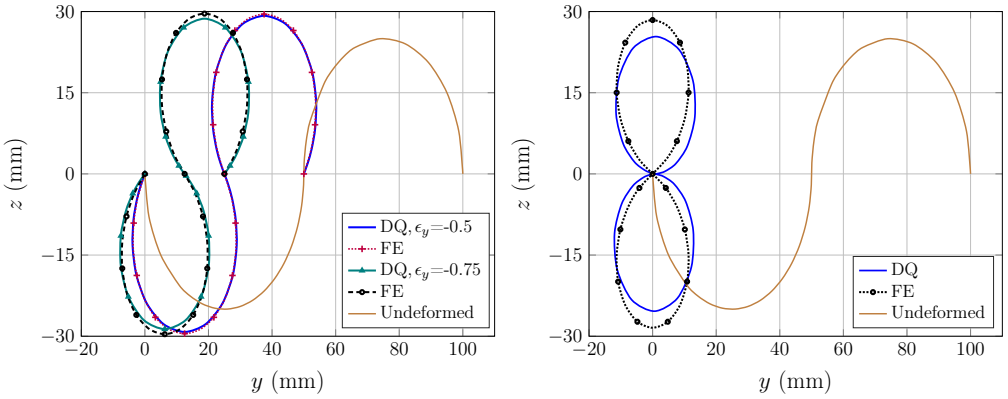


Figure 13: Deformed cross-section of a unit cell at different ϵ_y values in tension.

Similarly, in compression, the deformed cross-sections are shown in Figure 14. In all instances, the deformation patterns are consistent with FE results,

until a critical level of compression is achieved. As the strain increases from $\epsilon_y = -0.75$ to -1, the corrugated unit cell exhibits significantly larger rotations, causing the curvature displacement derivative relationship to be highly nonlinear. Hence, there is a noticeable discrepancy between the DQ result and the FE simulation. However, the DQ model still provides a reasonably accurate representation, offering a good approximation of the overall deformation pattern even under high compression. This ensures the capability of the DQ method to efficiently and accurately model highly deformable periodic structures, especially when computational cost is a concern.



(a) $\epsilon_y = -0.5$ and -0.75 **(b)** $\epsilon_y = -1$

Figure 14: Deformed cross-section of a unit cell at different ϵ_y values in compression.

6.4. Load case 3

In this case, the corrugated sheet is subjected to pure bending about the x or ξ axis with a constant curvature applied on both ends. All other membrane loads are zero. A fixed boundary condition at the center is used, such that the corrugated sheet undergoes symmetric deformation. The assumption that the displacement components v^0 and w^0 do not vary along the ξ direction is still valid. Consequently, the governing differential equations and DQ equations for load case 3 are the same as for load case 2 (Eq.27 and Eq.29 respectively), and the associated boundary conditions, including vanishing strain $\varepsilon_2^0 = 0$ and constant curvature, are given by:

$$
\begin{aligned}
&v^0(\eta = 2\,R\,\phi_0) = 0, && w^0(\eta = 2\,R\,\phi_0) = 0\\
&\varepsilon_1^1(\eta = 0) = -\epsilon_y^1, && \varepsilon_1^1(\eta = 4\,R\,\phi_0) = \epsilon_y^1\\
&\varepsilon_{2,2}^1 = 0, && \varepsilon_2^0 = 0\\
&\varphi_2(\eta = 2\,R\,\phi_0) = 0
\end{aligned}
\tag{31}
$$

where, φ_2 is rotation along the η axis and defined as:

$$
\varphi_2 = -\frac{\partial w^0}{\partial \eta} - \kappa v^0 \tag{32}
$$

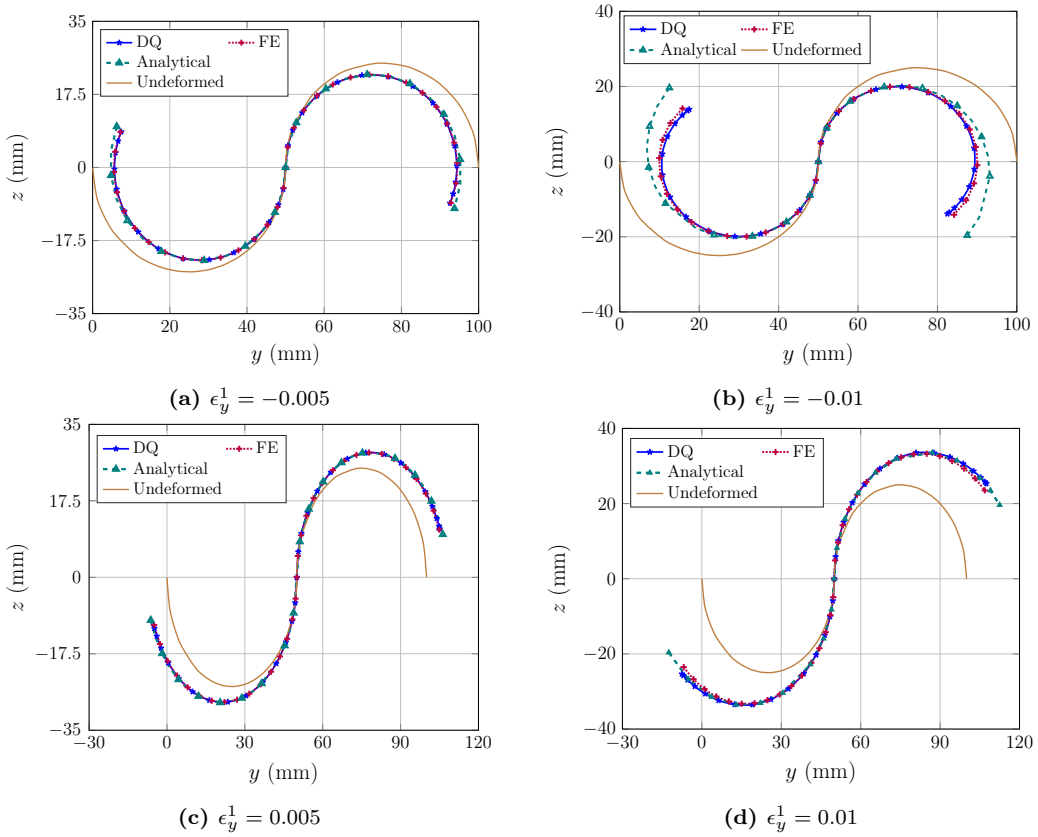
An odd number of grid points is chosen to apply a fixed boundary condition at the center of the unit cell. It should be noted that a δ point is required near the center to restrained the rotation, and it may be applied on either side of center. The vanishing strain and constant curvature boundary conditions can be applied at any grid point. However, they are enforced at the end grid points for convenience. The above boundary conditions in the DQ formulation are given as:

$$
\begin{aligned}
&v^0_{\{\frac{N}{2}\}+1} = 0, && w^0_{\{\frac{N}{2}\}+1} = 0\\
&\sum_{k=1}^{N} B^{(\eta)}_{1k}\, w^0_k + \kappa_1 \sum_{k=1}^{N} A^{(\eta)}_{1k}\, v^0_k = \epsilon_y^1, && \sum_{k=1}^{N} B^{(\eta)}_{Nk}\, w^0_k + \kappa_N \sum_{k=1}^{N} A^{(\eta)}_{Nk}\, v^0_k = -\epsilon_y^1\\
&\sum_{k=1}^{N} C^{(\eta)}_{1k}\, w^0_k + \kappa_1 \sum_{k=1}^{N} B^{(\eta)}_{1k} v^0_k = 0, && \sum_{k=1}^{N} A^{(\eta)}_{Nk} v^0_k - \kappa_N w^0_N +\\
&\frac{1}{2}\left[\left(\sum_{k=1}^{N} A^{(\eta)}_{Nk}\, v^0_k - \kappa_N\, w^0_N\right)^2 + \left(\sum_{k=1}^{N} A^{(\eta)}_{Nk}\, w^0_k + \kappa_N\, v^0_N\right)^2\right] = 0\\
&\sum_{k=1}^{N} A^{(\eta)}_{\{\frac{N}{2}\}-1\,k}\, w^0_k + \kappa_{\{\frac{N}{2}\}-1}\, v^0_{\{\frac{N}{2}\}-1} = 0
\end{aligned}
\tag{33}
$$

where $\{\}$ represent the integer division.

Figure 15 illustrates the deformed cross-section under various constant curvature ϵ_y^1, obtained using the DQ method with 19 grid points, FE simulations, and the analytical model proposed by Kress and Winkler [13]. Each subplot corresponds to a different applied curvature: $\epsilon_y^1 = \pm 0.005$

and $\epsilon_y^1 = \pm 0.01$. Under negative curvature, the corrugation bends inward toward the center of the unit cell. In contrast, positive curvature leads to a corresponding increase in the corrugation amplitude, resulting in a more pronounced corrugated profile. The undeformed configuration is also plotted for the reference.



(a) $\epsilon_y^1 = -0.005$ **(b)** $\epsilon_y^1 = -0.01$

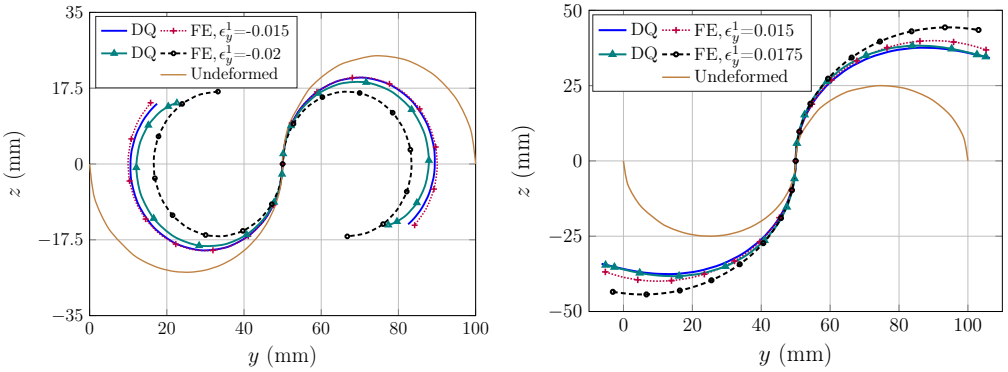
(c) $\epsilon_y^1 = 0.005$ **(d)** $\epsilon_y^1 = 0.01$

Figure 15: Deformed unit cell cross-sections from different models for load case 3.

The DQ results exhibit excellent agreement with both the FE simulations and the analytical solution for $\epsilon_y^1 = \pm 0.005$ (Figure 15 (a) and (c)), capturing the deformation in both positive and negative applied curvature regimes. As the applied curvature increases, the deformation of the unit cell becomes more pronounced, resulting in a noticeable inconsistency between the DQ and FE solutions and the existing analytical model. As shown in Figure 15 (b), this discrepancy is significant for negative applied curvature, particularly for $\epsilon_y^1 = -0.01$ and higher. In contrast, the deviation remains minimal under

positive applied curvature, with only a slight difference noted near the edges for $\epsilon_y^1 = 0.01$ as shown in Figure 15 (d).

Figure 16 depicts the deformed cross-sections for higher levels of applied curvature, only comparing the DQ method and FE simulations. The deformation becomes increasingly nonlinear as the magnitude of curvature increases in both positive and negative directions. Hence, the existing analytical solution is not plotted here. In the negative applied curvature case (Figure 16 (a)), the corrugation progressively flattens and folds inward, leading to an increasing discrepancy between the DQ and FE results. The deviation becomes more pronounced at $\epsilon_y^1 = -0.02$, where the DQ method slightly underpredicts the deformation. However, the corrugation amplitude increases significantly under negative curvature (Figure 16 (b)), and even in this case, the DQ model slightly underpredicts the deformation even for $\epsilon_y^1 = 0.0175$, particularly near the edges. Despite these deviations, the correlation between models remains reasonable, demonstrating the DQ method's capability to capture large deformations, albeit with some limitations at higher curvature levels due to the linear relation between curvature displacement derivatives assumed in the present study.



(a) $\epsilon_y^1 = -0.015$ and -0.02 **(b)** $\epsilon_y^1 = 0.015$ and 0.0175

Figure 16: Deformed cross-section of a unit cell at different applied curvature ϵ_y^1.

7. Linear and nonlinear equilibrium equations

A noticeable discrepancy is observed between the DQ and FE results in all load cases beyond a critical deformation. As mentioned earlier, the equilibrium equations for plates and shells, derived using the principle of

virtual work, depend upon the strain theory assumed to compute the strain energy. Hence, the observed disagreement may stem from the use of equilibrium equations derived from a linear analysis, despite the computation of stress resultants using a nonlinear stress-strain relationship. Therefore, a detailed study is conducted here to assess the impact of additional nonlinear terms (Eq.14) in the equilibrium equations. The equations, expressed in terms of stress resultants, are examined under three scenarios using the linear and nonlinear formulations. These scenarios include: (i) both the equilibrium equations and stress resultants are computed using the linear strain assumption; (ii) the equilibrium equations are derived using the linear strain theory, while the stress resultants are computed using the nonlinear stress-strain relation; and (iii) both the equilibrium equations and stress resultants are formulated using the nonlinear analysis. Scenario (i) is equivalent to the analytical solution obtained by Kress and Winkler [13], which is also included for comparison. Importantly, the linear relation between curvature and displacement derivatives (Eq.9) is used in all three scenarios.

The prescribed loading and boundary conditions for all load cases discussed above cause the displacements v^0 and w^0 to remain constant along the ξ direction, thus the equilibrium equations reduce to:

$$\begin{cases} \delta v^0: & \dfrac{\partial N_{22}}{\partial \eta} - \kappa \dfrac{\partial M_{22}}{\partial \eta} + \mathcal{O}(v^0, w^0) + p_2 = 0 \\ \delta w^0: & \dfrac{\partial^2 M_{22}}{\partial \eta^2} + \kappa N_{22} + \mathcal{P}(v^0, w^0) + q = 0 \end{cases} \tag{34}$$

where,

$$\begin{aligned} \mathcal{O}(v^0, w^0) &= \frac{\partial}{\partial \eta}\left(N_{22} \left\{ \frac{\partial v^0}{\partial \eta} - \kappa\, w^0 \right\} \right) + \kappa N_{22} \left\{ \frac{\partial w^0}{\partial \eta} + \kappa\, v^0 \right\} \\ \mathcal{P}(v^0, w^0) &= \frac{\partial}{\partial \eta}\left(N_{22} \left\{ \frac{\partial w^0}{\partial \eta} + \kappa\, v^0 \right\} \right) + \kappa N_{22} \left\{ \frac{\partial v^0}{\partial \eta} - \kappa\, w^0 \right\} \end{aligned} \tag{35}$$

$\mathcal{O}$ and $\mathcal{P}$ are only functions of v^0 and w^0 except for load case 1, where they also depend on the applied engineering strain ϵ_x. It is worth noting that the only reduced equations are solved even for load case 1.

Figure 17 illustrate the results obtained for all three scenarios for load case 1 at an applied engineering strain of $\epsilon_x = 0.725$. Only the deformed cross-section is shown for better comparison. As expected, the DQ solution for scenario (i) aligns well with the existing analytical model. The DQ solution

for scenario (iii), where the complete nonlinear equilibrium equation has been solved, does not significantly improve the result from scenario (ii), where the $\mathcal{O}(v^0, w^0)$ and $\mathcal{P}(v^0, w^0)$ terms are omitted while solving the nonlinear equilibrium equations. Evidently, the discrepancy between the DQ and FE results persists even when the full equations are used, ascertained that the mismatch arises solely from the assumption of linear curvature displacement derivatives.

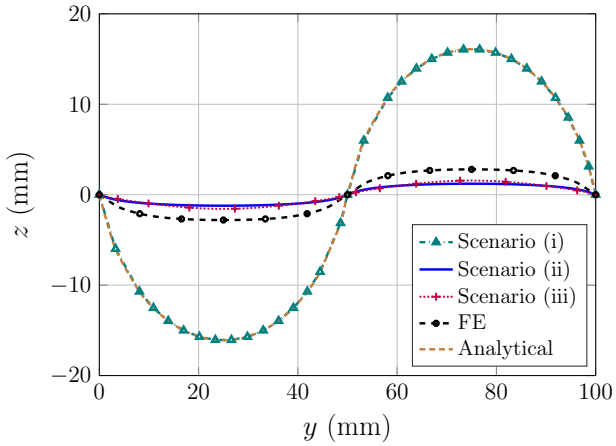
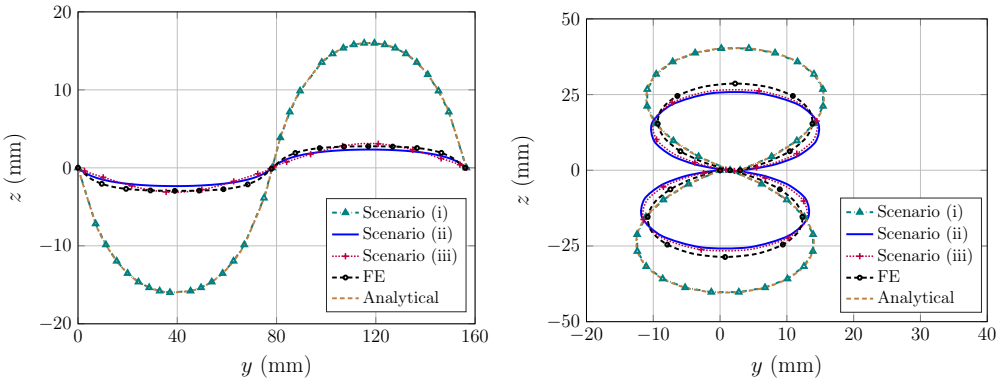


Figure 17: Deformed cross-section of unit cell under load case 1 for various scenarios at $\epsilon_x = 0.725$.

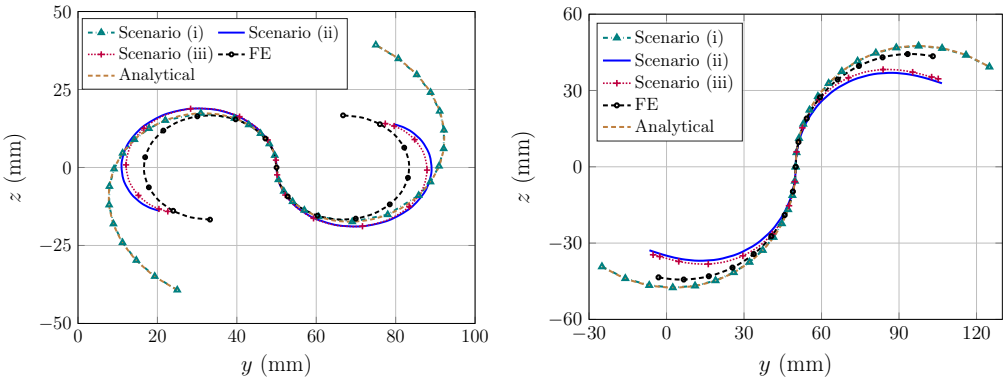
In addition, analyses are also carried out for load cases 2 and 3, and the results are shown in Figures 18 and 19, respectively. Notably, a convergence issue is observed while solving the resulting nonlinear equations with the DQ method using the Newton-Raphson technique for scenario (iii). Therefore, the results are presented for the maximum feasible converged strain levels: $\epsilon_y = 0.56$ in tension and $\epsilon_y = -0.97$ in compression. As can be seen, the DQ solution for scenario (i) aligns well with the existing analytical solution, while the solutions for scenarios (ii) and (iii) exhibit minimal differences in both tension and compression. A similar trend is observed for load case 3 (Figure 19) under both positive and negative curvature. The deformed cross-sections predicted by the DQ method for scenario (i) closely follow the existing analytical solution. Scenario (iii), which includes additional nonlinear terms, shows only minor differences, indicating the limited influence of these terms and remaining discrepancies with the FE results. These results further ensure that this discrepancy at moderately large rotation arises solely from the

assumption of a linear kinematic relation for curvature.



(a) $\epsilon_y = 0.56$ **(b)** $\epsilon_y = -0.97$

Figure 18: Deformed cross-section of unit cell under load case 2 for various scenarios.



(a) $\epsilon_y^1 = -0.02$ **(b)** $\epsilon_y^1 = 0.0175$

Figure 19: Deformed cross-section of unit cell under load case 3 for various scenarios.

8. Extension to complex corrugated configurations

A complex corrugation profile is considered as an example to demonstrate the validity of the DQ model over a wide range of geometries. Figure 20 shows the cross-section of the corrugated profile with $\phi_0 = 150°$. To maintain the same wavelength as the previous geometry, the radius is chosen as 50 mm. The analysis is carried out for all three load cases discussed earlier, and

the deformed shapes are presented here. It is worth noting that a higher number of grid points is required to accurately capture the deformed shape. Therefore, a total 29 grid points are chosen across the η direction, including δ points at boundaries, to obtain a smooth deformed shape.

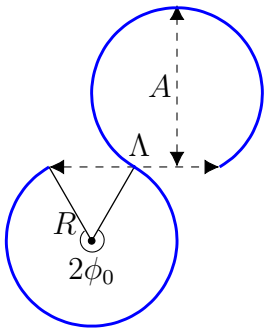


Figure 20: Cross-section profile of a corrugated unit cell.

The deformed configuration for load case 1 is illustrated in Figure 21 at engineering strain $\epsilon_x = 1$. As can be seen, the DQ result starts deviating from the FE prediction at $\epsilon_x = 1$ especially near the crest and the trough. These engineering strain levels are typically unrealistic for most materials. They are employed here solely to highlight the robustness of the DQ model.

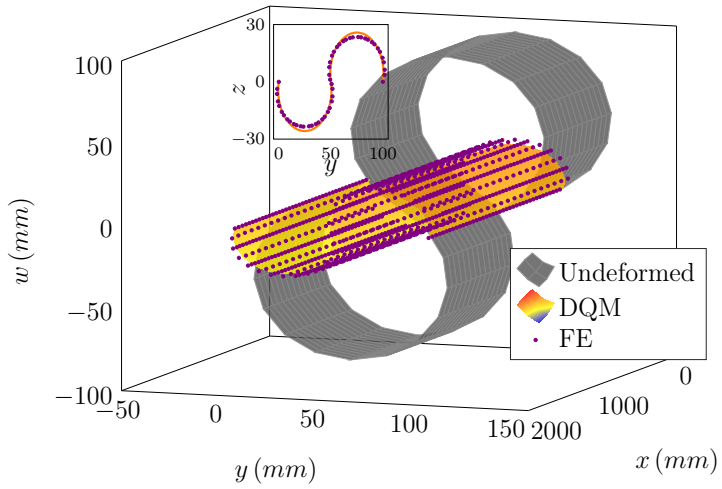


Figure 21: Deformed cross-section of unit cell for load case 1 at $\epsilon_x = 1$.

For all load cases, the DQ analysis is performed until a significant difference between the FE and DQ results is observed, except for the compression in load case 2, where the DQ analysis is restricted to $\epsilon_y = -1$. Notably, ϵ_y in the load case 2 is defined as strain with respect to the corrugation wavelength. Similar to the previous geometry, the true strain components ε^0_{11} and ε^0_{22} predicted from the DQ and FE models are compared in Figure 22. The DQ model closely follows the FE result, even for the complicated corrugated geometry, showing excellent agreement between the two numerical approaches.

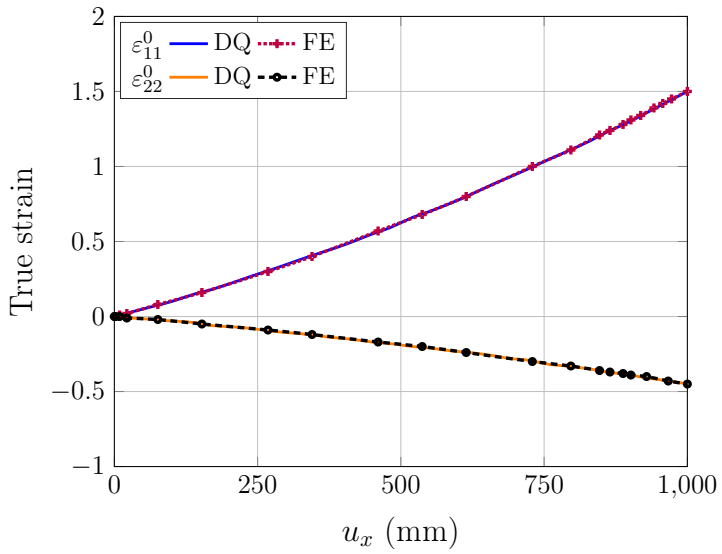
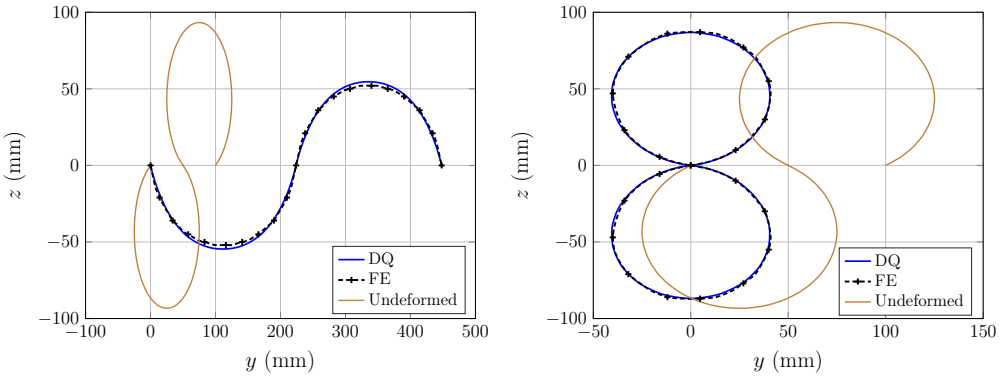


Figure 22: Comparison of true strain prediction using the DQ and FE methods..

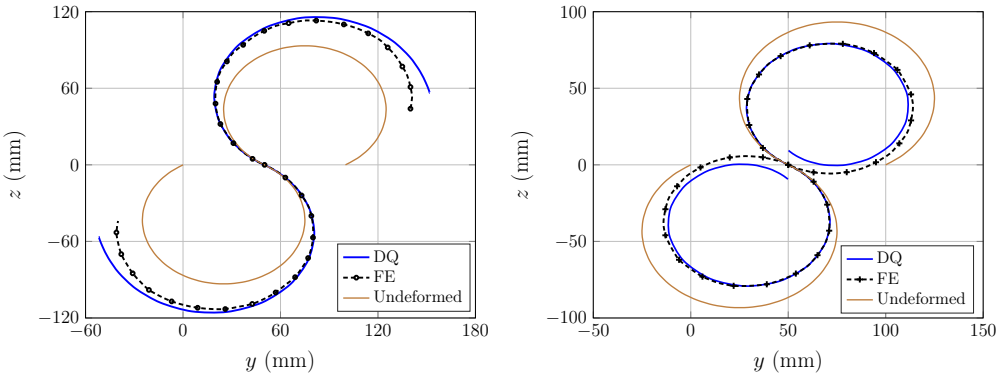
Figure 23 shows the corresponding deformed configurations for load case 2 at tensile and compressive strains of $\epsilon_y = 3.47$ and -1, respectively. Similar to load case 1, the discrepancies between the DQ and FE models in load case 2 are also noticeable near crest and trough regions. In compression, good agreement between these models is observed at $\epsilon_y = -1$. Similar analyses are performed for load case 3, where the deformed shapes at $\epsilon^1_y = \pm 0.0035$ are shown in Figure 24. Unlike other load cases, the discrepancy between the DQ and FE prediction results is more pronounced near both edges. Nevertheless, the DQ model demonstrates good agreement with the FE results over a wide range of deformations, even for the more complex corrugation profile. It is also evident that such complicated geometric configurations require a larger

number of grid points to accurately capture the deformation, which in turn increases the computational cost of the method.



(a) $\epsilon_y = 3.47$ **(b)** $\epsilon_y = -1$

Figure 23: Deformed cross-section of unit cell for load case 3 for various scenarios.



(a) $\epsilon_y^1 = 0.0035$ **(b)** $\epsilon_y^1 = -0.0035$

Figure 24: Deformed cross-section of unit cell under load case 3 for various scenarios.

9. Concluding remarks

This study presented a nonlinear formulation for the analysis of a thin circular corrugated sheet adopting the DQ method under various loading and boundary conditions. Three load cases are considered: two involved applied displacements along the x and y directions, respectively, while the third involves the application of a uniform curvature about the x or ξ axis. The

Euler-Lagrange equations are derived using the principle of virtual work and depends on the choice of strain and curvature. In the present study, nonlinear equilibrium equations are derived based on the Green-Lagrange strain and linearized curvature expression. The solutions obtained from the nonlinear analysis are compared with those from the linear analysis for two distinct scenarios. In the first instance, stress resultants are evaluated using the linear stress-strain relationship, and in the second scenario, they are computed using the nonlinear stress-strain formulation. These three scenarios are then investigated to evaluate the importance of the nonlinear terms in both equilibrium and kinematic equations for all load cases. The results demonstrated that the combination of equilibrium equations obtained from the linear analysis with stress resultant computed using the nonlinear kinematic relations is sufficient to accurately predict the deformed shape of a corrugated sheet, even in a significantly large deformation regime. For the simulations, an isotropic material is considered as a case study, reducing computational complexity. The governing equations are then formulated in terms of kinematic variables and material constants using the kinematic and constitutive relationships. The DQ results in the linear regime matched the existing analytical solution. The results demonstrated that while linear assumptions may suffice under small deformations, including nonlinear kinematics becomes essential for capturing the response under moderate to large deformations. Additionally, fully nonlinear FE analyses are performed to verify the DQ solution in both a small and large deformation regimes. The developed model accurately predicted responses up to a critical level of deformation for all load cases. Beyond this threshold, its underlying assumptions become invalid, requiring more advanced models that account for large rotations and a nonlinear curvature displacement relationship. This, however, will significantly increase the model's complexity and computational cost.

Future work may include applying this model to predict the deformed shape for load cases involving asymmetric loading or boundary conditions. Furthermore, this model can be extended to study orthotropic or anisotropic materials and moderately thick plates, making the approach applicable to a broader range of engineering problems, such as composite corrugated structures. Extending this model to explore the buckling response of corrugated sheets may also attract research interest. Furthermore, the DQ model can be easily extended to study the dynamic behaviour of such structures.

Acknowledgements

The authors gratefully acknowledge Dr. A. N. Roy Chowdhury (IIT Kanpur) for his insightful guidance and constructive suggestions that greatly contributed to this work.

Data Availability

The data produced in this research will be made available upon request.

Appendix A. Generalized equations for symmetric and orthotropic singly curved corrugated shells

The equilibrium equations for a singly-curved corrugated sheet for the linear analysis reduces to:

$$\begin{cases} \delta u^0\text{:} & \dfrac{\partial N_{11}}{\partial \xi} + \dfrac{\partial N_{12}}{\partial \eta} + \dfrac{\kappa}{2}\dfrac{\partial M_{12}}{\partial \eta} + p_1 = 0 \\ \delta v^0\text{:} & \dfrac{\partial N_{12}}{\partial \xi} + \dfrac{\partial N_{22}}{\partial \eta} - \dfrac{3\kappa}{2}\dfrac{\partial M_{12}}{\partial \xi} - \kappa\dfrac{\partial M_{22}}{\partial \eta} + p_2 = 0 \\ \delta w^0\text{:} & \dfrac{\partial^2 M_{11}}{\partial \xi^2} + 2\dfrac{\partial^2 M_{12}}{\partial \xi \partial \eta} + \dfrac{\partial^2 M_{22}}{\partial \eta^2} + \kappa N_{22} + q = 0 \end{cases} \tag{A.1}$$

where the stress resultants are evaluated using the Green-Lagrange strain and linear kinematic relation for curvature. For a symmetric and orthotropic laminate, the coupling matrix B_{ij} is zero and laminate is balanced, i.e., for specially orthotropic laminate, the A_{i6} and D_{i6} are also zero for $i = 1, 2$. Thus, the constitutive equation becomes:

$$\begin{bmatrix} N_{11} \\ N_{22} \\ N_{12} \\ M_{11} \\ M_{22} \\ M_{12} \end{bmatrix} = \begin{bmatrix} A_{11} & A_{12} & 0 & 0 & 0 & 0 \\ A_{12} & A_{22} & 0 & 0 & 0 & 0 \\ 0 & 0 & A_{66} & 0 & 0 & 0 \\ 0 & 0 & 0 & D_{11} & D_{12} & 0 \\ 0 & 0 & 0 & D_{12} & D_{22} & 0 \\ 0 & 0 & 0 & 0 & 0 & D_{66} \end{bmatrix} \begin{bmatrix} \varepsilon^0_{11} \\ \varepsilon^0_{22} \\ \gamma^0_{12} \\ \varepsilon^1_{11} \\ \varepsilon^1_{22} \\ \varepsilon^1_{12} \end{bmatrix} \tag{A.2}$$

On substituting stress resultants from the above equation into the governing differential equations (Eq.A.1), the equations can be expressed in terms

of kinematic variables and material constants as follows:

$$A_{11}\left[u^0_{,11}(1+u^0_{,1})+v^0_{,1}\,v^0_{,11}+w^0_{,1}\,w^0_{,11}\right]+A_{12}\left[(v^0_{,21}-\kappa\,w^0_{,1})(1+v^0_{,2}-\kappa\,w^0)+u^0_{,2}\,u^0_{,21}+(w^0_{,2}+\kappa\,v^0)(w^0_{,21}+\kappa\,v^0_{,1})\right]+A_{66}\left[u^0_{,22}(1+u^0_{,1})+v^0_{,12}(1+v^0_{,2}-\kappa w^0)+u^0_{,2}\,u^0_{,12}+v^0_{,1}(v^0_{,22}-\kappa w^0_{,2})+w^0_{,12}(w^0_{,2}+\kappa v^0)+w^0_{,1}(w^0_{,22}+\kappa v^0_{,2})\right]-0.5\,\kappa\,D_{66}\left[2w^0_{,122}+1.5\kappa\,v^0_{,12}-0.5\kappa u^0_{,22}\right]+p_1=0$$

$$A_{66}\left[u^0_{,21}(1+u^0_{,1})+v^0_{,11}(1+v^0_{,2}-\kappa w^0)+u^0_{,11}\,u^0_{,2}+v^0_{,1}(v^0_{,21}-\kappa w^0_{,1})+w^0_{,11}\,(w^0_{,2}+\kappa\,v^0)+w^0_{,1}\,(w^0_{,21}+\kappa\,v^0_{,1})\right]+A_{12}\left[u^0_{,12}(1+u^0_{,1})+v^0_{,1}\,v^0_{,12}+w^0_{,1}\,w^0_{,12}\right]+A_{22}\left[(v^0_{,22}-\kappa\,w^0_{,2})(1+v^0_{,2}-\kappa\,w^0)+u^0_{,2}\,u^0_{,22}+(w^0_{,2}+\kappa\,v^0)(w^0_{,22}+\kappa\,v^0_{,2})\right]+1.5\,\kappa\,D_{66}\left[2w^0_{,121}+1.5\,\kappa\,v^0_{,11}-0.5\,\kappa\,u^0_{,21}\right]+\kappa D_{12}[w^0_{,112}]+\kappa D_{22}[w^0_{,222}+\kappa v^0_{,22}]+p_2=0$$

$$-D_{11}\left[w^0_{,1111}\right]-D_{12}\left[2\,w^0_{,2211}+\kappa\,v^0_{,112}\right]-D_{22}[w^0_{,2222}+\kappa\,v^0_{,222}]-2D_{66}\left[2\,w^0_{,1212}+1.5\,\kappa\,v^0_{,112}-0.5\,\kappa\,u^0_{,212}\right]+\kappa\,A_{12}\left[u^0_{,1}+0.5\,\{(u^0_{,1})^2+(v^0_{,1})^2+(w^0_{,1})^2\}\right]+\kappa\,A_{22}\left[v^0_{,2}-\kappa\,w^0+0.5\,\{(u^0_{,2})^2+(v^0_{,2}-\kappa\,w^0)^2+(w^0_{,2}+\kappa\,v^0)^2\}\right]+q=0 \tag{A.3}$$

where 1 and 2 represent the ξ and η directions, respectively. A comma followed by subscripts denotes differentiation with respect to the subscripts. The displacements are assumed to be differentiable and have continuous second-order partial derivatives, allowing the differentiation order to be interchanged. Note that these equations can be easily generalized for composite materials by introducing the relevant coupling matrix terms. Figure 3 depicts the grid points on a unit cell to solve the above governing differential equations A.3 for a generalized load case. Both the global and local coordinate systems are shown on the grid. δ points near the boundaries are also shown to apply the Neumann boundary conditions in both the ξ and η directions. The total number of grid points is taken as N_1 and N_2 in the ξ and η directions, respectively. The local kinematic variables u^0, v^0, and w^0 can be obtained and transformed into global kinematic variables using the transformation (Eq.5) to obtain the displacement components u_x, u_y, and u_z.

In the differential quadrature method the above equations are written as:

$$A_{11}\left[\sum_{k=1}^{N_1} B_{ik}^{(1)} u_{kj}^0 \left(1+\sum_{k=1}^{N_1} A_{ik}^{(1)} u_{kj}^0\right)+\sum_{k=1}^{N_1} A_{ik}^{(1)} v_{kj}^0 \sum_{k=1}^{N_1} B_{ik}^{(1)} v_{kj}^0+\sum_{k=1}^{N_1} A_{ik}^{(1)} w_{kj}^0 \sum_{k=1}^{N_1} B_{ik}^{(1)} w_{kj}^0\right]+A_{12}\left[\left(\sum_{k=1}^{N_1}\sum_{l=1}^{N_2} A_{ik}^{(1)} A_{jl}^{(2)} v_{kl}^0-\kappa_{ij}\sum_{k=1}^{N_1} A_{ik}^{(1)} w_{kj}^0\right)\left(1+\sum_{l=1}^{N_2} A_{jl}^{(2)} v_{il}^0-\kappa_{ij} w_{ij}^0\right)+\sum_{l=1}^{N_2} A_{jl}^{(2)} u_{il}^0 \sum_{k=1}^{N_1}\sum_{l=1}^{N_2} A_{ik}^{(1)} A_{jl}^{(2)} u_{kl}^0+\left(\sum_{l=1}^{N_2} A_{jl}^{(2)} w_{il}^0+\kappa_{ij} v_{ij}^0\right)\left(\sum_{k=1}^{N_1}\sum_{l=1}^{N_2} A_{ik}^{(1)} A_{jl}^{(2)} w_{kl}^0+\kappa_{ij}\sum_{k=1}^{N_1} A_{ik}^{(1)} v_{kj}^0\right)\right]+A_{66}\left[\sum_{l=1}^{N_2} B_{jl}^{(2)} u_{il}^0\left(1+\sum_{k=1}^{N_1} A_{ik}^{(1)} u_{kj}^0\right)+\sum_{k=1}^{N_1}\sum_{l=1}^{N_2} A_{ik}^{(1)} A_{jl}^{(2)} v_{kl}^0\left(1+\sum_{l=1}^{N_2} A_{jl}^{(2)} v_{il}^0-\kappa_{ij} w_{ij}^0\right)+\sum_{l=1}^{N_2} A_{jl}^{(2)} u_{il}^0 \sum_{k=1}^{N_1}\sum_{l=1}^{N_2} A_{ik}^{(1)} A_{jl}^{(2)} u_{kl}^0+\sum_{k=1}^{N_1} A_{ik}^{(1)} v_{kj}^0\left(\sum_{l=1}^{N_2} B_{jl}^{(2)} v_{il}^0-\kappa_{ij}\sum_{l=1}^{N_2} A_{jl}^{(2)} w_{il}^0\right)+\sum_{k=1}^{N_1}\sum_{l=1}^{N_2} A_{ik}^{(1)} A_{jl}^{(2)} w_{kl}^0\left(\sum_{l=1}^{N_2} A_{jl}^{(2)} w_{il}^0+\kappa_{ij} v_{ij}^0\right)+\sum_{k=1}^{N_1} A_{ik}^{(1)} w_{kj}^0\left(\sum_{l=1}^{N_2} B_{jl}^{(2)} w_{il}^0+\kappa_{ij}\sum_{l=1}^{N_2} A_{jl}^{(2)} v_{il}^0\right)\right]-0.5\,\kappa_{ij}\,D_{66}\left[2\sum_{k=1}^{N_1}\sum_{l=1}^{N_2} A_{ik}^{(1)} B_{jl}^{(2)} w_{kl}^0+1.5\,\kappa_{ij}\sum_{k=1}^{N_1}\sum_{l=1}^{N_2} A_{ik}^{(1)} A_{jl}^{(2)} v_{kl}^0-0.5\,\kappa_{ij}\sum_{l=1}^{N_2} B_{jl}^{(2)} u_{il}^0\right]+p_1=0$$

$$A_{66}\left[\sum_{k=1}^{N_1}\sum_{l=1}^{N_2}A_{ik}^{(1)}A_{jl}^{(2)}u_{kl}^{0}\left(1+\sum_{k=1}^{N_1}A_{ik}^{(1)}u_{kj}^{0}\right)+\sum_{k=1}^{N_1}B_{ik}^{(1)}v_{kj}^{0}\left(1+\sum_{l=1}^{N_2}A_{jl}^{(2)}\right.\right.$$
$$\left.v_{il}^{0}-\kappa_{ij}w_{ij}^{0}\right)+\sum_{k=1}^{N_1}B_{ik}^{(1)}u_{kj}^{0}\sum_{l=1}^{N_2}A_{jl}^{(2)}u_{il}^{0}+\sum_{k=1}^{N_1}A_{ik}^{(1)}v_{kj}^{0}\left(\sum_{k=1}^{N_1}\sum_{l=1}^{N_2}A_{ik}^{(1)}A_{jl}^{(2)}v_{kl}^{0}\right.$$
$$\left.\left.-\kappa_{ij}\sum_{k=1}^{N_1}A_{ik}^{(1)}w_{kj}^{0}\right)+\sum_{k=1}^{N_1}B_{ik}^{(1)}w_{kj}^{0}\left(\sum_{l=1}^{N_2}A_{jl}^{(1)}w_{il}^{0}+\kappa_{ij}v_{ij}^{0}\right)+\sum_{k=1}^{N_1}A_{ik}^{(1)}w_{kj}^{0}\right.$$
$$\left.\left(\sum_{k=1}^{N_1}\sum_{l=1}^{N_2}A_{ik}^{(1)}A_{jl}^{(2)}w_{kl}^{0}+\kappa_{ij}\sum_{k=1}^{N_1}A_{ik}^{(1)}v_{kj}^{0}\right)\right]+A_{12}\left[\sum_{k=1}^{N_1}\sum_{l=1}^{N_2}A_{ik}^{(1)}A_{jl}^{(2)}u_{kl}^{0}\right.$$
$$\left(1+\sum_{k=1}^{N_1}A_{ik}^{(1)}u_{kj}^{0}\right)+\sum_{k=1}^{N_1}A_{ik}^{(1)}v_{kj}^{0}\sum_{k=1}^{N_1}\sum_{l=1}^{N_2}A_{ik}^{(1)}A_{jl}^{(2)}v_{kl}^{0}+\sum_{k=1}^{N_1}A_{ik}^{(1)}w_{kj}^{0}$$
$$\left.\sum_{k=1}^{N_1}\sum_{l=1}^{N_2}A_{ik}^{(1)}A_{jl}^{(2)}w_{kl}^{0}\right]+A_{22}\left[\left(\sum_{l=1}^{N_2}B_{jl}^{(2)}v_{il}^{0}-\kappa_{ij}\sum_{k=1}^{N_2}A_{jl}^{(2)}w_{il}^{0}\right)\left(1+\right.\right.$$
$$\left.\sum_{l=1}^{N_2}A_{jl}^{(2)}v_{il}^{0}-\kappa_{ij}w_{ij}^{0}\right)+\sum_{l=1}^{N_2}A_{jl}^{(2)}u_{il}^{0}\sum_{l=1}^{N_2}B_{jl}^{(2)}u_{il}^{0}+\left(\sum_{l=1}^{N_2}A_{jl}^{(2)}w_{il}^{0}+\kappa_{ij}v_{ij}^{0}\right)$$
$$\left.\left.\left(\sum_{l=1}^{N_2}B_{jl}^{(2)}w_{il}^{0}+\kappa_{ij}\sum_{l=1}^{N_2}A_{jl}^{(2)}v_{il}^{0}\right)\right]+1.5\kappa_{ij}D_{66}\left[2\sum_{k=1}^{N_1}\sum_{l=1}^{N_2}B_{ik}^{(1)}A_{jl}^{(2)}w_{kl}^{0}\right.\right.$$
$$\left.+1.5\kappa_{ij}\sum_{k=1}^{N_1}B_{ik}^{(1)}v_{kj}^{0}-0.5\kappa_{ij}\sum_{k=1}^{N_1}\sum_{l=1}^{N_2}A_{ik}^{(1)}A_{jl}^{(2)}u_{kl}^{0}\right]+\kappa_{ij}D_{12}\left[\sum_{k=1}^{N_1}\sum_{l=1}^{N_2}B_{ik}^{(1)}\right.$$
$$\left.A_{jl}^{(2)}w_{kl}^{0}\right]+\kappa_{ij}D_{22}\left[\sum_{l=1}^{N_2}C_{jl}^{(2)}w_{il}^{0}+\kappa_{ij}\sum_{l=1}^{N_2}B_{jl}^{(2)}v_{il}^{0}\right]+p_2=0$$

$$
\begin{aligned}
&- D_{11}\left[\sum_{k=1}^{N_1} D_{ik}^{(1)} w_{kj}^{0}\right] - D_{12}\left[2\sum_{k=1}^{N_1}\sum_{l=1}^{N_2} B_{ik}^{(1)} B_{jl}^{(2)} w_{kl}^{0} + \kappa_{ij}\sum_{k=1}^{N_1} B_{ik}^{(1)}\right. \\
&\left.\sum_{l=1}^{N_2} A_{jl}^{(2)} v_{kl}^{0}\right] - D_{22}\left[\sum_{l=1}^{N_2} D_{jl}^{(2)} w_{il}^{0} + \kappa_{ij}\sum_{l=1}^{N_2} C_{jl}^{(2)} v_{il}^{0}\right] - 2D_{66}\left[2\sum_{k=1}^{N_1}\sum_{l=1}^{N_2}\right. \\
&\left. B_{ik}^{(1)} B_{jl}^{(2)} w_{kl}^{0} + 1.5\kappa_{ij}\sum_{k=1}^{N_1}\sum_{l=1}^{N_2} B_{ik}^{(1)} A_{jl}^{(2)} v_{kl}^{0} - 0.5\kappa_{ij}\sum_{k=1}^{N_1}\sum_{l=1}^{N_2} A_{ik}^{(1)} B_{jl}^{(2)} u_{kl}^{0}\right] \\
&+ \kappa_{ij} A_{12}\left[\sum_{k=1}^{N_1} A_{ik}^{(1)} u_{kj}^{0} + 0.5\left(\sum_{k=1}^{N_1} A_{ik}^{(1)} u_{kj}^{0}\right)^2 + 0.5\left(\sum_{k=1}^{N_1} A_{ik}^{(1)} v_{kj}^{0}\right)^2 + 0.5\right. \\
&\left.\left(\sum_{k=1}^{N_1} A_{ik}^{(1)} w_{kj}^{0}\right)^2\right] + \kappa_{ij} A_{22}\left[\sum_{l=1}^{N_2} A_{jl}^{(2)} v_{il}^{0} - \kappa_{ij} w_{ij}^{0} + 0.5\left(\sum_{l=1}^{N_2} A_{jl}^{(2)} u_{il}^{0}\right)^2\right. \\
&\left. + 0.5\left(\sum_{l=1}^{N_2} A_{jl}^{(2)} v_{il}^{0} - \kappa_{ij} w_{ij}^{0}\right)^2 + 0.5\left(\sum_{l=1}^{N_2} A_{jl}^{(2)} w_{il}^{0} + \kappa_{ij} v_{ij}^{0}\right)^2\right] + q = 0 \\
&\qquad i = 3, 4, ..., N_1 - 2, \qquad j = 3, 4, ..., N_2 - 2
\end{aligned} \tag{A.4}
$$

References

[1] D. Dubina, V. Ungureanu, L. Gîlia, Cold-formed steel beams with corrugated web and discrete web-to-flange fasteners, Steel Construction 6 (2) (2013) 74–81.

[2] C. Ng, H. Zheng, Sound transmission through double-leaf corrugated panel constructions, Applied Acoustics 53 (1-3) (1998) 15–34.

[3] C.-C. Liang, M.-F. Yang, P.-W. Wu, Optimum design of metallic corrugated core sandwich panels subjected to blast loads, Ocean Engineering 28 (7) (2001) 825–861.

[4] E. Knox, M. Cowling, I. Winkle, Adhesively bonded steel corrugated core sandwich construction for marine applications, Marine structures 11 (4-5) (1998) 185–204.

[5] S.-H. Shin, D.-E. Ko, A study on minimum weight design of vertical corrugated bulkheads for chemical tankers, International Journal of Naval Architecture and Ocean Engineering 10 (2) (2018) 180–187.

[6] I. Dayyani, A. Shaw, E. S. Flores, M. Friswell, The mechanics of composite corrugated structures: A review with applications in morphing aircraft, Composite Structures 133 (2015) 358–380.

[7] C. Shan, J. Sun, Corrugated cylindrical shells: A review of structural type development and stability analysis methods, Thin-Walled Structures (2025) 113391.

[8] A. Norman, K. Seffen, S. Guest, Multistable corrugated shells, Proceedings of the Royal Society A: Mathematical, Physical and Engineering Sciences 464 (2095) (2008) 1653–1672.

[9] A. Norman, K. A. Seffen, S. D. Guest, Morphing of curved corrugated shells, International Journal of Solids and Structures 46 (7-8) (2009) 1624–1633.

[10] T. Yokozeki, S.-i. Takeda, T. Ogasawara, T. Ishikawa, Mechanical properties of corrugated composites for candidate materials of flexible wing structures, Composites Part A: applied science and manufacturing 37 (10) (2006) 1578–1586.

[11] W.-S. Chang, E. Ventsel, T. Krauthammer, J. John, Bending behavior of corrugated-core sandwich plates, Composite structures 70 (1) (2005) 81–89.

[12] C. Thill, J. A. Etches, I. P. Bond, K. D. Potter, P. M. Weaver, M. R. Wisnom, Investigation of trapezoidal corrugated aramid/epoxy laminates under large tensile displacements transverse to the corrugation direction, Composites Part A: Applied Science and Manufacturing 41 (1) (2010) 168–176.

[13] G. Kress, M. Winkler, Corrugated laminate homogenization model, Composite Structures 92 (3) (2010) 795–810.

[14] C. Thurnherr, L. Ruppen, G. Kress, P. Ermanni, Non-linear stiffness response of corrugated laminates in tensile loading, Composite Structures 157 (2016) 244–255.

[15] D. E. McFarland, An investigation of the static stability of corrugated rectangular plates loaded in pure shear. (1968).

[16] D. Briassoulis, Equivalent orthotropic properties of corrugated sheets, Computers & structures 23 (2) (1986) 129–138.

[17] O. A. Marzouk, G. Abdel-Sayed, Linear theory of orthotropic cylindrical shells, Journal of the Structural Division 99 (11) (1973) 2287–2306.

[18] I. Dayyani, S. Ziaei-Rad, H. Salehi, Numerical and experimental investigations on mechanical behavior of composite corrugated core, Applied Composite Materials 19 (2012) 705–721.

[19] A. Samanta, M. Mukhopadhyay, Finite element static and dynamic analyses of folded plates, Engineering structures 21 (3) (1999) 277–287.

[20] Y. Xia, M. I. Friswell, E. S. Flores, Equivalent models of corrugated panels, International journal of Solids and Structures 49 (13) (2012) 1453–1462.

[21] L. Peng, K. Liew, S. Kitipornchai, Analysis of stiffened corrugated plates based on the fsdt via the mesh-free method, International Journal of Mechanical Sciences 49 (3) (2007) 364–378.

[22] K. Liew, L. Peng, S. Kitipornchai, Nonlinear analysis of corrugated plates using a fsdt and a meshfree method, Computer Methods in Applied Mechanics and Engineering 196 (21-24) (2007) 2358–2376.

[23] H. Mohammadi, A. Setoodeh, A. Vassilopoulos, Isogeometric kirchhoff–love shell patches in free and forced vibration of sinusoidally corrugated fg carbon nanotube-reinforced composite panels, Thin-Walled Structures 171 (2022) 108707.

[24] H. Mohammadi, Isogeometric free vibration analysis of trapezoidally corrugated fg-grc laminated panels using higher-order shear deformation theory, in: Structures, Vol. 48, Elsevier, 2023, pp. 642–656.

[25] Y. Khalid, C. Chan, B. Sahari, A. Hamouda, Bending behaviour of corrugated web beams, Journal of materials processing technology 150 (3) (2004) 242–254.

[26] Z. Zhang, T. Qiu, R. Song, Y. Sun, Nonlinear finite element analysis of the fluted corrugated sheet in the corrugated cardboard, Advances in Materials Science and Engineering 2014 (1) (2014) 654012.

[27] R. Haj-Ali, J. Choi, B.-S. Wei, R. Popil, M. Schaepe, Refined nonlinear finite element models for corrugated fiberboards, Composite Structures 87 (4) (2009) 321–333.

[28] J. Park, S. Chang, H. M. Jung, Numerical prediction of equivalent mechanical properties of corrugated paperboard by 3d finite element analysis, Applied Sciences 10 (22) (2020) 7973.

[29] R. Bellman, B. Kashef, J. Casti, Differential quadrature: a technique for the rapid solution of nonlinear partial differential equations, Journal of computational physics 10 (1) (1972) 40–52.

[30] C. W. Bert, S. K. Jang, A. G. Striz, Two new approximate methods for analyzing free vibration of structural components, AIAA journal 26 (5) (1988) 612–618.

[31] H. Qing, L. Wei, Linear and nonlinear free vibration analysis of functionally graded porous nanobeam using stress-driven nonlocal integral model, Communications in Nonlinear Science and Numerical Simulation 109 (2022) 106300.

[32] M. Liao, Weak-form quadrature element method: A comparative review of different formulations and its comprehensive assessment, Archives of Computational Methods in Engineering 30 (1) (2023) 317–329.

[33] X. Wang, Nonlinear stability analysis of thin doubly curved orthotropic shallow shells by the differential quadrature method, Computer methods in applied mechanics and engineering 196 (17-20) (2007) 2242–2251.

[34] C. W. Bert, M. Malik, Differential quadrature method in computational mechanics: a review, Amencan Society of Mechanical Engineers (1996).

[35] S. Moradi, F. Taheri, Application of differential quadrature method to the delamination buckling of composite plates, Computers & structures 70 (6) (1999) 615–623.

[36] Y.-J. Hu, Y.-Y. Zhu, C.-J. Cheng, Dqem for large deformation analysis of structures with discontinuity conditions and initial displacements, Engineering Structures 30 (5) (2008) 1473–1487.

[37] B. Liu, C. Liu, S. Lu, Y. Wu, Y. Xing, A. Ferreira, A differential quadrature hierarchical finite element method using fekete points for triangles and tetrahedrons and its applications to structural vibration, Computer Methods in Applied Mechanics and Engineering 349 (2019) 798–838.

[38] H. M. Khalid, S. O. Ojo, P. M. Weaver, Inverse differential quadrature method for structural analysis of composite plates, Computers & Structures 263 (2022) 106745.

[39] Y. Tang, H. Qing, Size-dependent nonlinear post-buckling analysis of functionally graded porous timoshenko microbeam with nonlocal integral models, Communications in nonlinear science and numerical simulation 116 (2023) 106808.

[40] Y. Wang, R. Liu, X. Wang, On free vibration analysis of non-linear piezoelectric circular shallow spherical shells by the differential quadrature element method, Journal of Sound Vibration 245 (1) (2001) 179–185.

[41] X. Wang, Y. Wang, On non-linear behaviour of spherical shallow shells bonded with piezoelectric actuators by the differential quadrature element method (dqem), International Journal for Numerical Methods in Engineering 53 (6) (2002) 1477–1490.

[42] X. Wang, Y. Wang, Buckling analysis of thin rectangular plates under uniaxial or biaxial compressive point loads by the differential quadrature method, International journal of mechanical sciences 101 (2015) 38–48.

[43] T. Ng, L. Hua, K. Lam, C. Loy, Parametric instability of conical shells by the generalized differential quadrature method, International Journal for Numerical Methods in Engineering 44 (6) (1999) 819–837.

[44] K. Lam, H. Li, T. Ng, C. Chua, Generalized differential quadrature method for the free vibration of truncated conical panels, Journal of Sound and Vibration 251 (2) (2002) 329–348.

[45] T. Ng, H. Li, K. Lam, Generalized differential quadrature for free vibration of rotating composite laminated conical shell with various boundary conditions, International Journal of Mechanical Sciences 45 (3) (2003) 567–587.

[46] H. Qing, Y. Cai, Semi-analytical and numerical post-buckling analysis of nanobeam using two-phase nonlocal integral models, Archive of Applied Mechanics 93 (1) (2023) 129–149.

[47] K. Liew, T. Ng, J. Z. Zhang, Differential quadrature–layerwise modeling technique for three-dimensional analysis of cross-ply laminated plates of various edge-supports, Computer Methods in Applied Mechanics and Engineering 191 (35) (2002) 3811–3832.

[48] J. Z. Zhang, T. Ng, K. Liew, Three-dimensional theory of elasticity for free vibration analysis of composite laminates via layerwise differential quadrature modelling, International Journal for Numerical Methods in Engineering 57 (13) (2003) 1819–1844.

[49] J. N. Reddy, Theory and analysis of elastic plates and shells, CRC press, 1999.

[50] J. N. Reddy, Mechanics of laminated composite plates and shells: theory and analysis, CRC press, 2003.

[51] R. Bellman, J. Casti, et al., Differential quadrature and long-term integration, Journal of mathematical analysis and Applications 34 (2) (1971) 235–238.

[52] X. Wang, C. Bert, A new approach in applying differential quadrature to static and free vibrational analyses of beams and plates, Journal of Sound Vibration 162 (3) (1993) 566–572.

[53] G. Karami, P. Malekzadeh, A new differential quadrature methodology for beam analysis and the associated differential quadrature element method, Computer Methods in Applied Mechanics and Engineering 191 (32) (2002) 3509–3526.

[54] Y. Wang, C. Feng, J. Yang, D. Zhou, S. Wang, Nonlinear vibration of fg-gplrc dielectric plate with active tuning using differential quadrature method, Computer Methods in Applied Mechanics and Engineering 379 (2021) 113761.

[55] X. Wang, Differential quadrature and differential quadrature based element methods: theory and applications, Butterworth-Heinemann, 2015.

[56] C. Shu, Differential quadrature and its application in engineering, Springer Science & Business Media, 2012.

[57] A. Sherbourne, M. Pandey, Differential quadrature method in the buckling analysis of beams and composite plates, Computers & Structures 40 (4) (1991) 903–913.

[58] B. He, X. Wang, Error analysis in differential quadrature method, Transactions of Nanjing University of Aeronautics and Astronautics (1994) 194–200.

[59] A. S. U. Manual, Abaqus 6.11, http://130.149 89 (2080) (2012) v6.

[60] V. V. Novozhilov, Foundations of the nonlinear theory of elasticity, Courier Corporation, 1999.

[61] M. Amabili, A comparison of shell theories for large-amplitude vibrations of circular cylindrical shells: Lagrangian approach, Journal of Sound and Vibration 264 (5) (2003) 1091–1125.